The Effect of a Weak Asthenospheric Layer on Surface Kinematics, Subduction Dynamics and Slab Morphology in the Lower Mantle

Nestor G. Cerpa, Karin Sigloch, Fanny Garel, Arnauld Heuret, D. Rhodri Davies, Mitchell Mihalynuk

To cite this version:

Nestor G. Cerpa, Karin Sigloch, Fanny Garel, Arnauld Heuret, D. Rhodri Davies, et al.. The Effect of a Weak Asthenospheric Layer on Surface Kinematics, Subduction Dynamics and Slab Morphology in the Lower Mantle. Journal of Geophysical Research : Solid Earth, 2022, 127 (8), pp.e2022JB024494. 10.1029/2022JB024494 . hal-03764872

HAL Id: hal-03764872
https://hal.umontpellier.fr/hal-03764872

Submitted on 30 Aug 2022

HAL is a multi-disciplinary open access archive for the deposit and dissemination of scientific research documents, whether they are published or not. The documents may come from teaching and research institutions in France or abroad, or from public or private research centers.

L'archive ouverte pluridisciplinaire **HAL**, est destinée au dépôt et à la diffusion de documents scientifiques de niveau recherche, publiés ou non, émanant des établissements d'enseignement et de recherche français ou étrangers, des laboratoires publics ou privés.

The effect of a weak asthenospheric layer on surface kinematics, subduction dynamics and slab morphology in the lower mantle

Nestor Cerpa[1], Karin Sigloch[2], Fanny Garel[1], Arnauld Heuret[3], D. Rhodri Davies[4], Mitchell G. Mihalynuk[5]

[1]Geosciences Montpellier, University de Montpellier, CNRS, Université des Antilles, Place Eugène Bataillon, 34095 Montpellier, France

[2]Geoazur, Université Côte d'Azur, CNRS, Observatoire de la Côte d'Azur, IRD, 250 Avenue Albert Einstein, 06560 Valbonne, France

[3]Université de Guyane, Géosciences Montpellier, 97300, Cayenne, France

[4]Research School of Earth Sciences, The Australian National University, Canberra, ACT, 2601, Australia

[5]British Columbia Geological Survey, PO Box 9333 Stn Prov Govt, Victoria, British Columbia V8W 9N3, Canada

Key Points:

- Tectonic plate kinematics and seismic tomography suggest slab accumulation in the mantle transition zone, beneath near-stationary trenches.
- By contrast, subduction dynamics models tend to produce inclined, laterally extended slabs associated with slab rollback and trench retreat.
- Adding a sub-lithospheric weak layer accelerates subduction, limits trench migration, and promotes sub-vertical slab piles, as observed.

Corresponding author: Nestor Cerpa, `nestor.cerpa@umontpellier.fr`

Abstract

On Earth, the velocity at which subducting plates are consumed at their trenches (termed 'subduction rate' herein) is typically 3 times higher than trench migration velocities. The subduction rate is also 5 times higher than estimated lower mantle slab sinking rates. Using simple kinematic analyses, we show that if this present-day "kinematic state" operated into the past, the subducting lithosphere should have accumulated and folded beneath near-stationary trenches. These predictions are consistent with seismic tomography, which images localized and widened lower-mantle slab piles. They are, however, at odds with most dynamic-subduction models, which predict rapid trench retreat and inclined slabs in the mantle transition zone. We test the hypothesis that a weak asthenospheric layer (WAL), between the lithosphere-asthenosphere boundary and 220 km depth, compatible with geophysical constraints, can remedy the discrepancies between numerical models and observations. The WAL lubricates the base of the lithosphere, increases the subduction rate while reducing trench retreat. As a consequence, simulations featuring a WAL predict slab accumulation at the mantle transition zone, and thicker, folded slabs in the lower mantle. A WAL viscosity only 2-5 times lower than that of the adjacent mantle is sufficient to shift subduction regimes towards a mode of vertical slab sinking and folding beneath near-stationary trenches, across a wide range of model parameters, producing surface and slab velocities close to those observed at the present-day. These findings provide support for the existence of a weak asthenosphere beneath Earth's lithosphere, complementing independent evidence from various geophysical data.

Plain Language Summary

At convergent margins (subduction zones, marked by deep trenches), oceanic (subducting) plates plunge into Earth's mantle. Analysis of the present-day surface velocities suggest that subducting plates are consumed at trenches at rates of 5 cm/yr, on average. Moreover, it is observed that the consumption rate is higher than the trench migration velocity, which is often less than 1 cm/yr. At depth below 660 km, marking the transition from the upper to the lower mantle, the subducted piece of the plate (the slab) encounters increased resistance to its sinking, with slab sinking velocities at these depths being less than about 1.5 cm/yr. Take together, such rapid plate consumption at quasi-fixed trenches, along with slab deceleration in the lower mantle, causes a "traffic jam" leading to sub-vertical accumulation of the slab and folding. This behavior is confirmed by seismic imaging techniques of Earth's interior which reveals vertically-sinking piles of oceanic slabs at and beneath a 660-km depth. However, computational and laboratory models of subduction zones often fail to reproduce these first-order observations. Here, we demonstrate that the addition of a lubricating mantle layer at the base of the oceanic plates reduces the mismatch between the aforementioned observations and predictions from 2-D computation models.

1 Introduction

The negative buoyancy of subducting plates is a primary driving force sustaining subduction and surface plate motions (Forsyth & Uyeda, 1975). Subduction zones are the sites of tectonically-forced horizontal deformation (Uyeda & Kanamori, 1979; Lallemand et al., 2005) and dynamic vertical motions (G. Davies, 1981; Gurnis, 1993). Crust and lithosphere subducting beyond the mantle transition zone add chemical heterogeneities to the lower mantle, which are stirred and homogenised by mantle convection (Zindler & Hart, 1986; Jones et al., 2016), or persist to the core-mantle-boundary, as suggested by modern tomographic models (e.g. Hosseini et al., 2020). Understanding the deep dynamics of subducting slabs is thus key for addressing the geodynamical and geochemical evolution of our planet.

Observed plate kinematics provide insights into the dynamics of the subduction system (Forsyth & Uyeda, 1975; Jarrard, 1986; Lallemand et al., 2005; Heuret & Lallemand, 2005; Sdrolias & Müller, 2006; Doglioni et al., 2007; Funiciello et al., 2008; Schellart, 2008b; Becker & Faccenna, 2009; Goes et al., 2011). Subduction kinematics (see Fig. 1) involve the velocities of the subducting plate v_{sp} ("SP velocity" for short); the velocity of the overriding plate v_{op} ("OP velocity"); and the velocity of the trench v_t, which is equal to OP velocity if the overriding plate does not undergo (back-arc) deformation. Note that v_{sp} and v_t are defined with opposite signs: the natural (positive) direction of trench migration is "retreat" towards the SP. These absolute velocities are given in some absolute reference frame, which is taken as the stable lower mantle herein (Becker & Faccenna, 2009).

The subduction rate v_s is the velocity of the subducting plate relative to the trench (i. e., the rate at which the subducting plate is consumed by the migrating trench). It has been repeatedly shown that typical values of v_s on Earth are higher than 3-4 cm/yr (Forsyth & Uyeda, 1975; Jarrard, 1986), while absolute trench motions are usually between -2 and 2 cm/yr (Heuret & Lallemand, 2005; Funiciello et al., 2008; Schellart, 2008b). Other studies have pointed out that the magnitude of the (absolute) SP velocity v_{sp} is generally two to three times higher than that of the (absolute) v_t (Becker & Faccenna, 2009; Goes et al., 2011; Carluccio et al., 2019). Hence plates are consumed at much faster rates than their trenches move laterally.

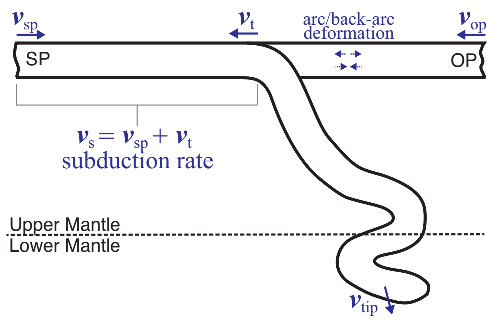

Figure 1. a) Sketch illustrating the various kinematics that can be inferred within a subduction system. Positive values denote absolute trenchward motion for both the subducting plate (v_{sp}) and the overriding plate (v_{op}). Absolute trench velocity (v_t) is considered positive towards the subducting plate. We define relative to a fixed lower-mantle reference frame, in order to compare to absolute motions in nature, which can be quantified in empirical, approximate mantle reference frames, such as the fixed-hotspot frame. Subduction velocity (v_s) is a relative velocity, the rate at which the subducting plate is consumed at the trench ($v_s = v_{sp} + v_t$).

Analogue and numerical models of subduction dynamics without external forcing (hereafter simply referred to as models of subduction dynamics) have shed light on the internal force balance of subduction systems and the resulting kinematics. They have illuminated various subduction regimes and slab morphologies in the upper mantle (e. g. Guillou-Frottier et al., 1995; Schellart, 2008a; Di Giuseppe et al., 2008; Ribe, 2010; Stegman et al., 2010). Recent studies that included an overriding plate with finite strength, concluded that the slab pull force associated with the negative buoyancy of a subducting plate (SP) favored slab rollback and migration of the trench towards the subducting plate (i. e., trench retreat), unless the SP was weak and/or the overriding plate (OP) was strong (Garel et al., 2014; Sharples et al., 2014; A. Holt et al., 2015; Hertgen et al., 2020). It has been pointed out that such analogue and numerical models of subduction dynamics tend to produce surface kinematics that are at odds with some of the first-order observations outlined above (Goes et al., 2011; Carluccio et al., 2019). These subduction models generally produce trench retreat velocities that exceed present-day observations, especially once the subducting slab reaches the bottom of the upper mantle, which was sometimes treated as a rigid barrier (Funiciello et al., 2004; Schellart, 2005; Capitanio et al., 2007; Goes et al., 2011). More modest trench motions over a relatively wide range of parameters have only been produced by 2-D models that consider both the penetration of the subducting slab into the lower mantle and complex rheologies (Garel et al., 2014; A. Holt et al., 2015; Z.-H. Li et al., 2019). Even then, slower trench motion is only achieved at the cost of decreasing the SP velocity to values of less than 2 cm/yr once the slab interacts with the viscosity increase around 660-km depth (hereafter referred to as "first slab-660 interaction") (e.g. Garel et al., 2014; Suchoy et al., 2021). Hence, in most subduction dynamics models, more than half of the subduction rate v_{sp} is accounted for by trench motion v_t, which contradicts present-day observations of plate kinematics.

Independent constraints on subduction dynamics come from seismic tomographic images of slab morphologies at and below the mantle transition zone. A few slabs under present-day subduction zones in the Western Pacific appear to stagnate above the 660-km discontinuity (Karason & Van Der Hilst, 2000; Amaru, 2007; C. Li et al., 2008; Fukao & Obayashi, 2013) - for instance, under Japan (Fukao et al., 1992) and under Izu-Bonin (Wu et al., 2016), at least under its northernmost part (Zhang et al., 2019). But many other slabs have breached the 660-km discontinuity and are sinking into the lower mantle (Goes et al., 2017). Transition-zone and lower-mantle slabs are imaged more robustly and consistently than slabs in the upper(most) mantle. The opposite would be expected if slabs retained a constant thickness across depths. Hence the deeper slab must be thicker (Ribe et al., 2007; Loiselet et al., 2010), which is well-documented under the Americas (Karason & Van Der Hilst, 2000; Ren et al., 2007; Sigloch & Mihalynuk, 2013; Mohammadzaheri et al., 2021), but also globally (Van der Voo et al., 1999; Shephard et al., 2017; Van der Meer et al., 2018; Hosseini et al., 2020). Under the particularly well-instrumented Cascadia subduction zone of North America, tomography can resolve a shallow slab of single lithospheric thickness, and also confidently show that the slab is multiply thickened from the transition zone downward (Sigloch et al., 2008).

Thickened slabs in the lower mantle have been attributed to slab buckling and folding through the mantle transition zone (Ricard et al., 1993; Guillou-Frottier et al., 1995; Ribe et al., 2007; Běhounková & Čížková, 2008; Lee & King, 2011; Cerpa et al., 2014; Billen & Arredondo, 2018), with possible slab detachment (Čížková et al., 2012). Slab folds have not yet been resolved by tomography, so the exact widening mechanism remains speculative from the observational side.

Some numerical subduction models have produced vertical slab folding by imposing a fixed overriding plate, i.e., trench velocity $v_t = 0$ (e.g. Lee & King, 2011). Models with mobile plates often predict trench-retreat modes while sub-vertical slab folding tends to be limited to simulations with relatively young subducting plates and old overriding plates (Garel et al., 2014; T. Yang et al., 2018; Strak & Schellart, 2021; Behr et al., 2022), or to double-subduction set-ups (Čížková & Bina, 2015; Lyu et al., 2019). By contrast, the tomographic observations – of pervasively thickened lower-mantle slabs, concentrated in narrow, linear belts – suggest that slab folding beneath largely stationary trenches should prevail across a wide range of subduction settings. Thus we argue that current subduction models may lack a first-order ingredient that favors (almost) vertically stacked, thick lower-mantle slabs, which tends to be observed independently of plate strength and/or the distance to other subduction zones. Phase transitions at 410 and 660 km can produce realistic lower-mantle slab morphologies by altering slab sinking rates (Briaud et al., 2020; Čížková & Bina, 2013; Arredondo & Billen, 2017), although the required Clapeyron slopes may be too extreme (see e.g. Agrusta et al., 2017, and references therein). Hence there is room for considering alternative mechanisms.

To summarize, there are at least two discrepancies between existing models of subduction dynamics and first-order observations. First, current models generally produce trench retreat velocities v_t in excess of those observed at present-day subduction zones, alongside SP velocities v_{sp} and subduction rates v_s that are too slow after first slab-660 interaction. Second, models seldom reproduce the tomographically observed, multiply thickened geometries that prevail in the transition zone and lower mantle.

This study considers how a weak asthenospheric layer (WAL) beneath the plate can resolve these discrepancies. The presence of a WAL on Earth has been proposed to explain a large range of geophysical observations, including lithospheric net rotation (Ricard et al., 1991), postglacial rebound and gravity data (e.g. Paulson & Richards, 2009), shear-wave tomography (Kawakatsu et al., 2009; Barruol et al., 2019), seismic attenuation (Y. Yang et al., 2007; Debayle et al., 2020), seismic anisotropy (Montagner & Tanimoto, 1991; Debayle & Ricard, 2013; Becker, 2017) and electrical conductivity tomography (Naif et al., 2013). The viscosity reduction could originate from a plume-fed asthenosphere (Phipps Morgan et al., 1995), from the depth-dependency of dislocation creep flow laws (Raterron et al., 2011), from crystal-preferred orientation (Meyers & Kohlstedt, 2021), or from the presence of melt pockets (Cooper & Kohlstedt, 1986; Chantel et al., 2016), which may remain trapped due to low melt fractions (Holtzman, 2016) or low density contrast (Sakamaki et al., 2013).

The presence of a WAL is predicted to affect large-scale dynamics of the underlying, convecting mantle (Lenardic et al., 2006), and to favor 'plate-like' rather than 'stagnant-lid' regimes (Höink et al., 2012). Since the sub-lithospheric mantle resists a plate's trenchward motion, the inclusion of a WAL in models of subduction dynamics yields faster subduction velocities v_{sp}, as shown by Carluccio et al. (2019) and Suchoy et al. (2021). The latter authors also showed that increased v_{sp} was coeval with reduced trench retreat v_t, although they did not detail the implications for lower mantle slab morphologies. We hypothesize that increasing subduction rates while reducing trench motion results in the accumulation of slab material in a near-vertical column beneath the (quasi stationary) trench, and that the slab must widen (through folding) around the depths where it slows down to lower-mantle sinking rates, given that slab input v_s remains high. Thus, a WAL could resolve both first-order discrepancies regarding plate velocities and slab morphologies.

We carry out a systematic numerical analyses of how a WAL impacts the dynamics of thermo-mechanical subduction models featuring an overriding plate. Section 2 provides a first-order quantification of slab widening behavior in modern subduction zones, using plate kinematic data. Section 3 describes the model setup. Section 4 presents our modeling results, and Section 5 discusses their implications for subduction systems on Earth.

2 Quantifying slab folding from plate motions and slab sinking rates

2.1 Conceptual assessment

We start by demonstrating how slab folding can be assessed theoretically as a geometrical/kinematic phenomenon, involving slab accumulation in the mantle transition zone. This analysis is inspired by subduction models where (unlike our own model) velocities are applied to one or both plates, and which can predict slab morphology as a function of these imposed surface kinematics (Christensen, 1996; Heuret et al., 2007; Arcay et al., 2008; Gibert et al., 2012; Cerpa et al., 2015; Guillaume et al., 2018; Cerpa et al., 2018). Among these, Gibert et al. (2012), anchored the subducting slab to a rigid 660-km discontinuity, which aims to simulate the effect of a strong viscosity jump at 660 km, as inferred from e.g. geodetic constraints (B. H. Hager, 1984; B. Hager & Richards, 1989; Mitrovica & Forte, 2004). Gibert et al. (2012) showed that if the subduction rate

$v_s = v_{sp} + v_t$ exceeds the trench velocity v_t, continued subduction results in slab folding at the base of the upper mantle. Essentially, the slab has to fold because trench retreat does not create enough lateral accommodation space to permit all incoming slab to lie down flat on the '660'. Here we extend their analysis to the more general case where the subducting slab sinks into the lower mantle.

Let $v_s \times \Delta t$ be the length of subducted material consumed at the trench over some duration Δt. The lateral displacement of the trench over the same duration is $v_t \times \Delta t$. The displacement of the deepest portions of the subducting slab (simplified as the displacement of the slap tip) within the upper mantle is approximated as $v_{\text{tip}} \times \Delta t$, where v_{tip} is the absolute velocity of the deepest point of the slab. Slab folding can thus be understood as a simple geometrical constraint. When the length of subducted material is larger than the lateral displacement of the trench plus the displacement of the slab tip, the excess length (slab accumulation) is expected to be accommodated by folding. Put in another form, slab accumulation and folding occurs when:

length of subducted material > trench displacement + slab tip motion in the mantle

Alternatively, we can define a kinematic ratio K_r which predicts whether the subducting slab undergoes folding as:

$$K_r = \frac{v_s}{|v_t| + \sqrt{(v^x_{\text{tip}})^2 + (v^z_{\text{tip}})^2}} \tag{1}$$

where we have decomposed the velocity of the deepest point of the slab into its horizontal and vertical components.

When $K_r \simeq 1$, the free space created by trench retreat and slab sinking can accommodate all newly incoming lithosphere, which does not have to compress (fold). Hence the slab's apparent thickness remains similar in the upper and lower mantle (Fig. 2). A kinematic ratio K_r higher than 1 implies a surplus of slab material that cannot be accommodated by trench retreat and slab sinking into the lower mantle, and instead has to be accommodated by slab folding. At $K_r > 1$, the higher the value of K_r, the greater the frequency of slab folds (or alternatively, the wider the amplitude of the folds). Also at $K_r > 1$, the apparent thickness of the folded slab in the lower mantle is predicted to be multiples of the lithospheric thickness observed in the uppermost mantle.

The ratio of trench velocity to slab-sinking velocity (v_t/v^z_{tip}) controls, to first order, the average slab dip. This is true for both the unfolded ($K_r \leq 1$) and folded ($K_r >$

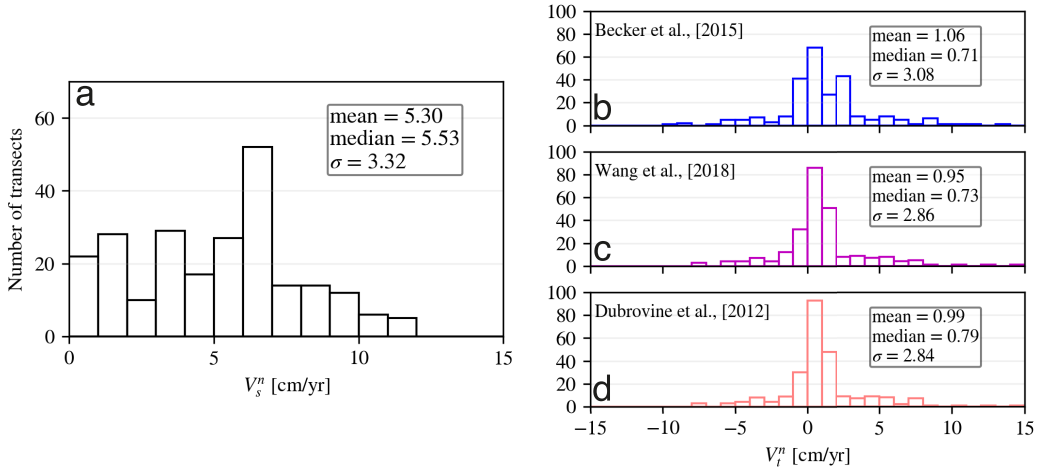

Figure 2. Range of theoretically possible geometries for slabs that sank vertically after entering the trench and have penetrated well into the lower mantle (LM). Dashed lines mark the viscosity discontinuity between upper mantle (UM) and LM, in this study assumed to equate to the seismic "660-km discontinuity". The x-axis plots the ratio of trench motion to the slab's(approximate) sinking velocity. v_t is absolute trench velocity and v^z_{tip} is the vertical velocity component of the deepest slab tip (approximating the slab's overall sinking rate). Positive values of v_t/v^z_{tip} represent trench retreat, negative values trench advance. A stationary trench ($v_t/v^z_{tip} = 0$) leads to a vertical slab piling up beneath it; a migrating trench results in a dipping slab. The y-axis plots the kinematic ratio (K_r, Eq. 1) which expresses whether the length of slab newly entering the mantle (per time unit) can be accommodated in the slab-free space created by trench migration (horizontally away from the slab) and/or by the sinking of older motion of the slab (which vacates upper-mantle space). $K_r > 1$ indicates a shortfall of newly created accommodation space, so that the slab must fold (or thicken in some other way) in order to adjust.

1) cases. Note that we use only the vertical component of the slab-tip velocity as it is thought to be much higher than the horizontal component (see also below section 2.2).

Hence the parameter space along the dimensions of K_r and v_t/v^z_{tip} spans a variety of candidate slab morphologies and subduction regimes, as depicted in (Fig. 2). For negative trench motion (trench advance), the subducting slab leans forward, so that the deepest slab portions lie beneath the subducting plate at increasing distances from the trench (leftmost regimes in Fig. 2). For quasi-null trench motions, the subducting slab sinks vertically, with all slab portions remaining below the trench. For relatively high, positive trench motions (trench "retreat"), the subducting slab leans backwards (" slab rollback"), with deeper slab beneath the overriding plate. It has been proposed that high trench-retreat rates promote the complete stagnation of slab atop the 660-km discontinuity (Torii & Yoshioka, 2007; Goes et al., 2017), so that high values of v_t/v^z_{tip} may lead to the end-member subduction regime where the slab flattens and folds on the 660-km discontinuity (rightmost regimes in Fig. 2).

2.2 Estimating slab folding at present-day

In order to gauge the prevalence of slab folding in nature, we seek to calculate an observational estimate of K_r in active subduction zones, using Equation 1. Hence we need estimates of subduction rate v_s, absolute trench velocity v_t, and slab sinking velocity v_{tip}.

For estimating v_s and v_t, we use an updated version of the SUBMAP database (Lallemand et al., 2005), which defines 249 transects of active subduction zones. Subduction rates are retrieved from the relative plate motions of the MORVEL56-NNR model (based on a circuit of 56 tectonic plates (Argus et al., 2011) as explained in the Supplementary Information Text S1). Each SUBMAP subduction transect is assigned to a subducting plate and an overriding plate of the MORVEL56-NNR plate circuit. For transects that cross significant arc and back-arc deformation, MORVEL56-NNR permits the definition of an "arc block" and assessment of trench motion relative to that of a rigid overriding plate, enhancing the accuracy of the derived subduction rate. For a few subduction zones, the MORVEL56-plate circuit does not account for active arc and back-arc deformation even though such a deformation has been well-established in the literature (Southernmost-Central Andes, Izu-Bonin, Calabria). For these transects, we complement MORVEL56-NNR with published regional studies (see Supplementary Information).

To define the absolute motion of the plates and trenches, we need to consider an absolute plate motion model within an absolute reference frame, comparable to the fixed reference frame of our numerical models. In this paper we calculate and compare the value of K_r in three recent absolute plate motion models, constructed in different manners: the "SA" ("spreading-alignement") model (Becker et al., 2015), the "TM25" model (Wang et al., 2018), and the "GMHRF-1Ma" model by Doubrovine et al. (2012). The SA model minimizes the angular misfit between spreading-ridge orientations and plate velocities. This plate motion was found to give a good fit to azimuthal seismic anisotropy, a proxy for the shear induced by the relative motion between the tectonic plates and the upper mantle. The TM25 model is based on 25 hotspot tracks under the assumption of fixed hotspots relative to the deep mantle. The GMHRF-1Ma model is based on a global fit of hotspot tracks since the Late Cretaceous, accounting for modest relative motions between the hotspots' mantle plumes, computed by numerical models of whole mantle convection.

We extract the trench-normal component of the plates and trench velocities for comparison with our 2-D models. In what follows, the absolute and relative velocities at each transect are those of their trench-normal components.

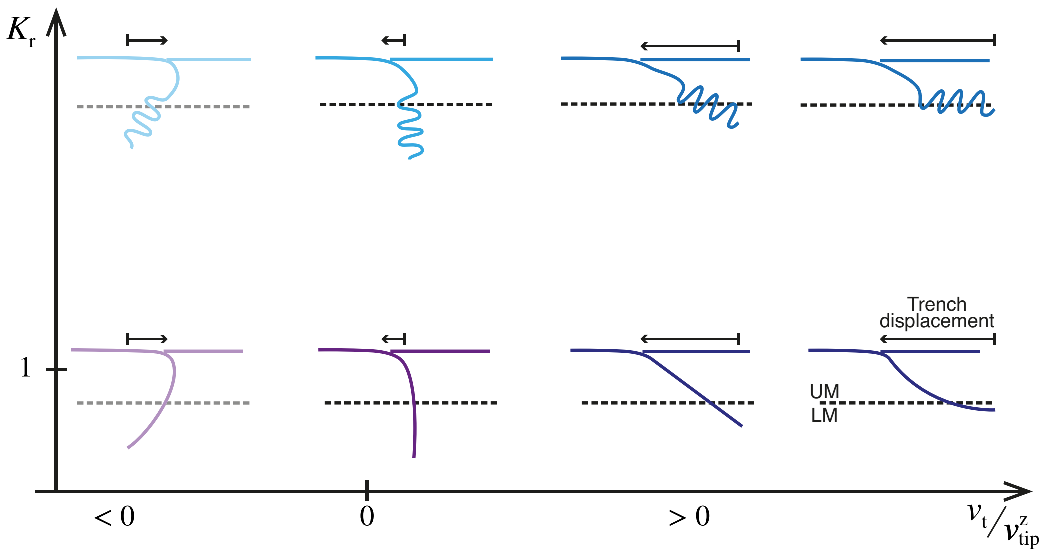

Figure 3. a) Histogram of the trench-normal component of subduction rate v_s in present-day subduction zones. b Histogram of the trench-normal component of trench velocity (retreat) v_t, in the spreading-alignment reference frame (Becker et al., 2015). c) Histogram as in b) but for T25M reference frame (Wang et al., 2018). d) Like b), but for GMHRF-1Ma frame (Doubrovine et al., 2012).

The observed subduction rates are non-negative with a median value of 5.3 cm/yr and a long tail up to almost 12 cm/yr (Fig. 3a). In all three reference frames (Fig. 3b-d), absolute trench velocity v_t scatters around slightly positive values with a median values of 0.71 to 0.79 cm/yr. This tendency towards slow trench retreat may or may not be significantly different from zero motion (stationary trench), given the large formal standard deviations of almost 3 cm/yr but also the non-Gaussian, heavy tails of the histogram.

In any case, two thirds of the subduction transects have trench velocities between -1 and 1 cm/yr in the three absolute plate motion frames. Hence typical present-day trench motion is roughly five times smaller than typical subduction velocities.

Estimating K_r also requires an estimate of slab sinking rates in the lower mantle. In principle, the reduction of slab sinking rate from UM to LM could be derived from the viscosity contrast between upper and lower mantle (Richards, 1991; Ricard et al., 1993). Given the rheology uncertainties and variability of slab sinking rates across the upper mantle, we prefer to use estimates based on tomographic observations. Since imaged slabs are not directly dateable, they have been correlated to the geology of accretionary orogens, which hold the surface record of subduction. The subduction of lithosphere is accompanied by the formation of a volcanic arc at the surface, which often survives and is dateable. Such slab-arc correlations have inferred time-averaged sinking rates of 1.0-1.5 cm/yr for slabs that have penetrated the lower mantle (Van Der Meer et al., 2010; Sigloch & Mihalynuk, 2013; Domeier et al., 2016; Van der Meer et al., 2018; Mohammadzaheri et al., 2021).

Using 1.0 cm/yr as the slab sinking velocity estimate, 70–80% of subduction transects exhibit values of $K_r > 1$ in all three absolute reference frames (Fig. 4 and Fig. S1). Only a few subduction transects consistently display $K_r < 1$ in all reference frames, mostly at the edges of longer arcs: the southernmost Andes (Patagonian transects), the northern edge of the Lesser Antilles (e.g. Puerto Rico Trench), or the edges of the South Sandwich SZ.

The present-day prevalence of $K_r > 1$ is relatively insensitive to the assumed slab sinking velocity. Even when considering $v_{tip} = 1.5$ cm/yr, at the high end of the reasonable estimate range (see e.g. Butterworth et al., 2014; Domeier et al., 2016)), 63% of transects remain above $K_r > 1$ in the spreading-aligned absolute plate motion model, and 72% of transects in the two other reference frames.

Figure 4a plots the global inventory of slabs (between 600-1800 km depth), from which the sinking rates were derived. Importantly, most areas are slab free. Existing slabs cluster in two vast, linear belts: one under the Alpine-Eurasian-Himalayan-southwest Pacific orogens; the second under the Americas and into Siberia. From the geologic record and quantitative plate reconstructions, these are the known, absolute locations of major orogenies over the past 200 million years, hence the known paleo-trench locations.

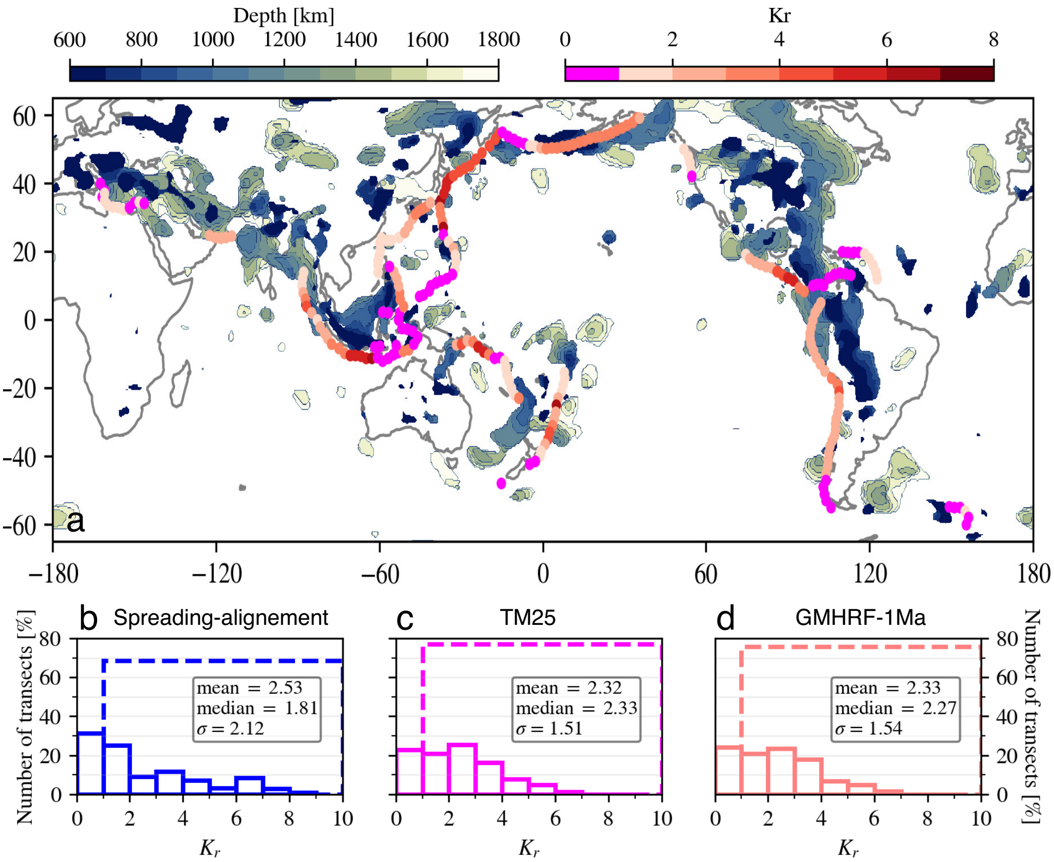

Figure 4. a) Map shows estimates of the kinematic ratio K_r (reddish color scale) for all subduction transects of the SUBMAP database (Heuret & Lallemand, 2005). The regime of inferred slab folding ($K_r > 1$) prevails in most subduction zones. The absolute plate motion model is GMHRF-1Ma, which yields intermediate K_r values compared to the also-investigated spreading-alignment and TM25 models (plotted on Fig. S1 in the supplementary information). Also shown in blue shades is the global inventory of subducted slabs in the lower mantle (600-1800 km depth). More precisely, these are contours of seismically fast P-velocity anomalies exceeding dvp/vp>0.35% in global model DETOX-P2 (Hosseini et al., 2020). b) Histogram of K_r values in the spreading-alignment reference frame. c) Histogram of K_r values in the TM25 reference frame. d) Histogram of K_r values in the GMHRF-1Ma reference frame.

The observation that slabs are still located only beneath these independently inferred paleo-trench regions means that slabs sank rather vertically. The vast slab-free mantle areas are known not to have hosted trenches over the past 200 m.y. This implies that paleo-trenches have remained quite stationary over a time period during which the area equivalent of all ocean basins was subducted once or twice over (Coltice et al., 2012). Thus trenches had the opportunity to migrate across the globe but did not, which indicates sustained $K > 1$ (slab folding regime) over geologic time.

Finally, slab dimensions directly point towards folding. In figure 4a, the Eurasian and American slab belts are 15,000-20,000 km long; individual slab segments are 1,000-3,000 km long (i.e., arc length) and 400-700 km wide. The latter is a multiple of lithospheric thickness, and suggests slab folds of this amplitude.

Thus three separate lines of observational reasoning suggest that most present and past subduction zones feature(d) a surplus of subducted material not accommodated by lateral trench migration and slab sinking, so that instead slab folding is required. As discussed, common models of subduction dynamics (hereafter referred to as standard models) seldom reproduce this regime. Next we investigate whether adding a WAL to a standard model can shift its regimes from non-folding to folding over a wide range of model parameters.

3 Modeling approach

We use 2-D thermo-mechanical models of subduction dynamics. The governing equations are those suitable for multi-material, incompressible viscous flow, under the Boussinesq approximation, which are solved using the finite-element, control-volume, unstructured adaptive mesh Fluidity computational modelling framework, which has been carefully validated for simulations of this nature (D. R. Davies et al., 2011; S. Kramer et al., 2012; Le Voci et al., 2014; S. C. Kramer et al., 2021). Our model setup and material properties are similar to Garel et al. (2014), albeit that in some cases we extend the models by incorporating a sub-lithospheric weak asthonospheric layer (WAL), similar to that in Suchoy et al. (2021). Our models neglect the potential effects of phase transitions on the buoyancy forces. Below we summarize our modeling approach.

3.1 Model Setup

The model predicts the evolution of a single subduction zone comprising both a subducting plate (SP) and an overriding plate (OP), with no external forces or velocities applied to the system. The model domain is a Cartesian box that is 8000-km wide and 2900-km in height (i.e. the whole mantle depth). Mechanical boundary conditions on the sides and base of the domain are free-slip, with a free-surface at the top. We use

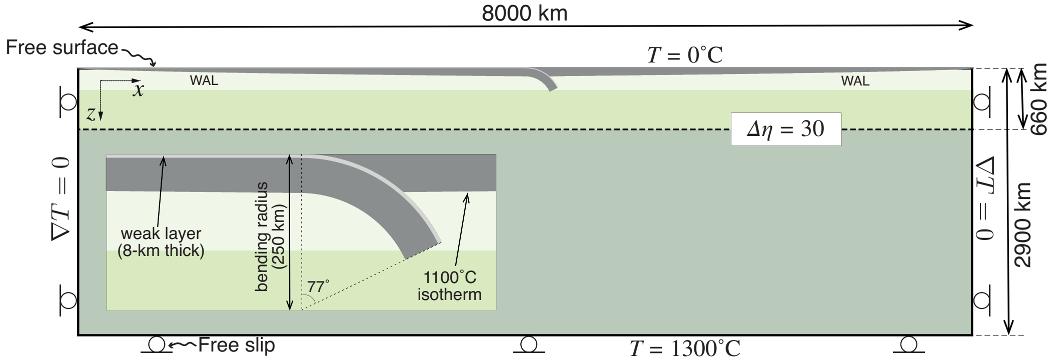

Figure 5. Model setup and boundary conditions. In the standard models the viscosity of the WAL is equal to that of ambient mantle ($\alpha = 1$), i.e., no weak asthenospheric layer (WAL) is present. The initial curved geometry of the subducting plate is prescribed using a bending radius of 250 km, including the weak layer.

no-flux thermal boundary conditions on the sides and impose constant temperatures of 0°C and 1300°C at the surface and at the bottom boundaries, respectively.

The initial temperature field is given by a half-space cooling model where the age of the plates vary linearly from the 0 at the ridges to (A_{SP}) for the subducting plate and to (A_{OP}) for the overriding plate. Models begin with a curved subducting slab to initiate subduction (see inset Fig. 5). Two mid-ocean ridges are initially set at either end of the model box, and are subsequently free to move according to the model dynamics.

We consider a composite visco-plastic rheology that accounts for four deformation mechanisms: linear diffusion creep, and non-linear dislocation creep, Peierls creep and pseudo-brittle yielding. The effective viscosity is:

$$\frac{1}{\eta_{eff}} = \left(\frac{1}{\eta_{diff}} + \frac{1}{\eta_{disl}} + \frac{1}{\eta_P} + \frac{1}{\eta_Y} \right) \tag{2}$$

which is bounded at lower (10^{18} Pa s) and upper (10^{25} Pa s) limits.

The diffusion (η_{diff}), dislocation (η_{disl}) and Peierls (η_{P}) viscosities follow the generic form:

$$\eta_{\text{diff|disl|P}} = A^{\frac{1}{n}} \exp\left(\frac{E + PV}{nRT_r} \right) \dot{\epsilon}_{II}^{\frac{1-n}{n}} \tag{3}$$

where A is a prefactor, n is the stress exponent, E and V are the activation energy and volume, respectively. P is the lithostatic pressure, R the gas constant, and $\dot{\epsilon}_{II}$ the second invariant of the strain-rate tensor. T_r is the sum of model temperature and an adiabatic temperature gradient of 0.5 °C/km and of 0.3 °C/km in the upper and lower mantle, respectively. The pseudo-brittle yielding viscosity follows a yield-stress law

$$\eta_Y = \frac{\tau_Y}{2\dot{\epsilon}_{II}} \tag{4}$$

where the yield strength $\tau_Y = \min(\tau_0 + f_c P, \tau_Y^{\max})$, with τ_0 the surface yield strength, f_c the friction coefficient, P the lithostatic pressure, and $\tau_Y^{\max}$ the maximum yield strength. The interface weak layer is 8-km thick, with a friction coefficient 10 times lower than the mantle material, and a maximum prescribed viscosity of 10^{20} Pa s. We impose a viscosity contrast $\Delta\eta$ of 30 at a 660-km depth between upper and lower mantle (B. H. Hager, 1984; Gurnis & Hager, 1988; Ricard et al., 1993; Čadek & Fleitout, 1999; Mitrovica & Forte, 2004). All rheological parameters are listed in Table 1.

3.2 Treatment of WAL

The depth extent of a potential WAL is not well constrained. Some studies, which consider it to be a layer of partial melt, suggest that it is only 10-20 km thick (Schmerr, 2012; Sakamaki et al., 2013; Stern et al., 2015), whereas others advocate for a layer extending from the lithosphere-asthenosphere boundary up to 200-300 km depth (thus a thickness of approximately 100-200 km) (Kawakatsu et al., 2009; Paulson & Richards, 2009; French et al., 2013; Becker, 2017; Barruol et al., 2019; Debayle et al., 2020). Here, we simulate the presence of the WAL by imposing a viscosity reduction between the 1100 °C isotherm (a proxy for the LAB) and a depth of 220 km, similarly to Suchoy et al. (2021). Note that models tested with a WAL extending up to 300 km depth showed little differences with the results reported below. We define the effective viscosity within the WAL as:

$$\eta_{\mathrm{WAL}} = \alpha\eta_{\mathrm{eff}} \tag{5}$$

where $0 < \alpha \leq 1.0$ is a reduction-viscosity factor.

The viscosity reduction of a WAL, and its origin, is also debated. For example, partial melt can lead to a 20-fold or larger viscosity reduction (Holtzman, 2016), but strongly depends on melt fraction, creep regime, grain size and wetting angle (Kohlstedt & Zimmerman, 1996). Milder viscosity reduction (< 5-fold) are expected from crystal-preferred orientation considerations (Meyers & Kohlstedt, 2021). We explore α values of 1.0 (no viscosity reduction – standard case); 0.5 (two-fold weaker asthenosphere – WAL case); and 0.2 (five-fold weaker – pronounced WAL case)). Note that larger viscosity reductions (α in the range 0.01–0.1) have usually been used in global mantle flow models reproducing sub-plate seismic anisotropy (Conrad & Behn, 2010; Becker, 2017). In our models with a composite rheology, shearing in the sub-plate mantle produces additional weakening of the strained layer relative to the underlying ambient mantle, by the sole effect of dislocation creep. Thus a nominal reduction factor of $\alpha = 0.2$ to 0.5 may produce actual viscosity reductions by one order of magnitude (see e.g. the viscosity profile in Fig. S10). Empirically, values of α lower than 0.1 in our set-up led to unrealistically large surface velocities >50 cm/yr very early in the simulations.

4 Model results

We first perform a set of simulations without a WAL ($\alpha = 1$), that we hereafter refer to as standard cases. Next, we explore sets of simulations with different degrees of weakening in the WAL (i.e. various values of α), that we refer to as WAL cases. For each case, we define a reference simulation (with plate ages $A_{sp} = 40$ My and $A_{op} = 20$ My). We subsequently run simulations that span a range of initial ages to cover a wide range of strength and buoyancy for both plates, while being representative of all regions of the subduction regime diagram presented in Garel et al. (2014).

4.1 Standard cases - no WAL

4.1.1 Reference simulation [$A_{sp} = 40$ My;$A_{op} = 20$ My]

Figure 6 displays the temporal evolution of the reference simulation for the standard cases ($\alpha = 1$). We focus on the evolution of the surface kinematics and the viscosity field in the sub-plate mantle (i.e., the uppermost upper mantle which undergo relatively high shear stresses and which is found between the cold lithosphere and depths of up to a 300-km depth). The velocity profile along the plates corresponds to "plate-like behavior": the velocity is constant except in the trench region, where both plates undergo deformation (Figure S3). Since trench velocity is very similar to OP velocity, indicating little back-arc deformation at all stages of the models, we will only describe the evolution in terms of trench velocity.

During the first stage of free sinking through the upper mantle (Fig. 6a), the subducting plate accelerates as slab pull increases with increasing slab length. It reaches a peak velocity of ~ 13 cm/yr with trench retreat/OP velocity peaking at ~ 4 cm/yr (Fig. 6g).

Table 1. Physical parameters used in the simulations, unless stated otherwise. UM and LM stand for upper and lower mantle, respectively.

Quantity	Symbol	Units	Value
Gravity	g	m s^{-2}	9.8
Thermal expansivity coefficient	α	K^{-1}	3 10^{-5}
Thermal diffusivity	κ	m^2 s^{-1}	10^{-6}
Reference density	ρ_s	kg m^{-3}	3300
Cold, surface temperature	T_s	K	273
Hot, mantle temperature	T_m	K	1573
Gas constant	R	J K^{-1} mol^{-1}	8.3145
Max. viscosity	$\eta_{\max}$	Pa s	10^{25}
			10^{20} (WI)
Max. viscosity interplate layer	$\eta_{\max,\mathrm{weak}}$	Pa s	10^{20}
Min. viscosity	$\eta_{\min}$	Pa s	10^{18}
Diffusion creep			
Activation energy	E	kJ mol^{-1}	300 (UM)
			200 (LM)
Activation volume	V	cm^3 mol^{-1}	4 (UM)
			1.5 (LM)
Prefactor	A	Pa^{-1} s^{-1}	3.0 10^{-11} (UM)
			6.0 10^{-17} (LM - $\Delta\eta = 30$)
	n	-	1
Dislocation creep (UM)[a]			
Activation energy	E	kJ mol^{-1}	540
Activation volume	V	cm^3 mol^{-1}	12
Prefactor	A	Pa^{-n} s^{-1}	5.0 10^{-16}
	n	-	3.5
Peierls mechanism creep (UM)[a]			
Activation energy	E	kJ mol^{-1}	540
Activation volume	V	cm^3 mol^{-1}	10
Prefactor	A	Pa^{-n} s^{-1}	10^{-150}
	n	-	20
Yield strength law			
Surface yield strength	τ_0	MPa	2
Friction coefficient	f_c	-	0.2
	$f_{c,\mathrm{weak}}$	-	0.02 (weak layer)
Maximum yield strength	$\tau_{y,\max}$	MPa	10 000

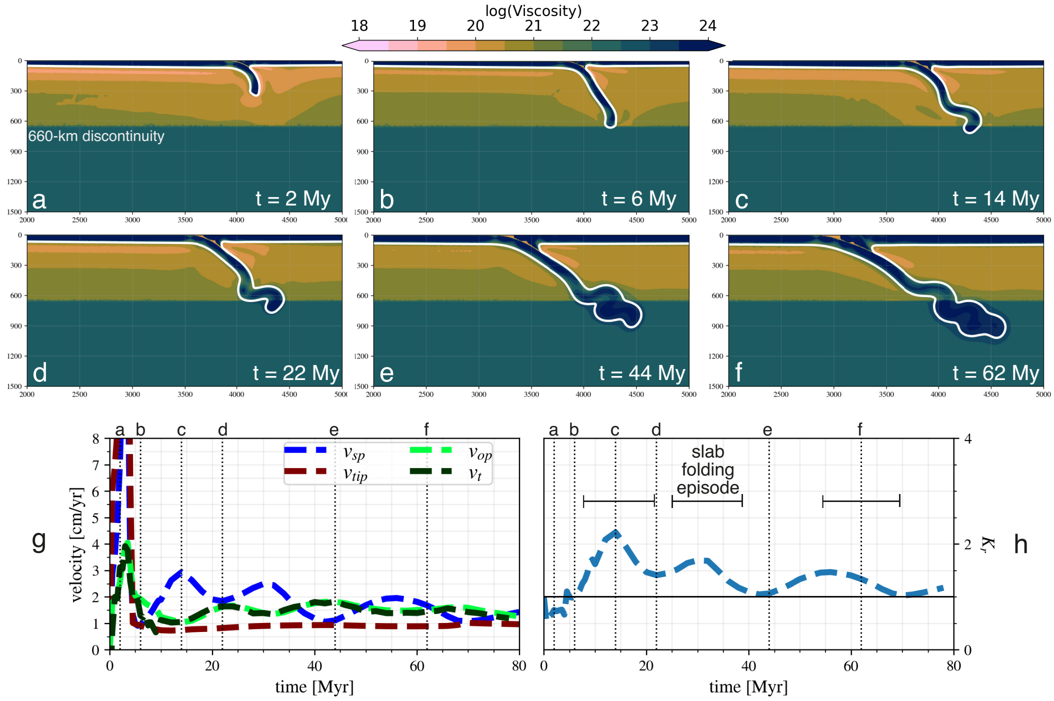

Figure 6. Reference standard model, featuring $A_{sp} = 40$ and $A_{op} = 20$ My. (a-f) Temporal snapshots of the evolution of the viscosity field, from 2 My to 62 My. The white line gives the 1100°C-isocontour. g) Kinematics of plates, slab, and trench. v_{sp} in dark blue, positive to the right. v_{op} in green, positive to the left. v_t in light blue, positive to the left. v_{tip} in dark red is the magnitude of slab tip velocity in. Vertical dashed lines mark snapshots times of (a-f). h) Temporal evolution of Kinematic ratio K_r, a proxy for the slab's propensity to fold (definition in the text). Horizontal black line denotes the boundary between the folding ($K_r > 1$) versus non-folding ($K < 1$) regime.

429 The fast SP motion induces high shear stresses in the underlying asthenosphere. This
430 causes high sub-plate strain rates, which favors dislocation creep and lower viscosity than
431 in the less-sheared, underlying mantle. The same occurs within the mantle wedge be-
432 low 200 km depth, where high strain rates are due to corner flow. Away from these high-
433 strain rate regions, diffusion creep dominates (see e.g. Garel et al., 2014).

434 As soon as the slab tip encounters the high-viscosity lower mantle around $t \simeq 5$
435 My, plate velocities decrease to between 1 and 3 cm/yr. The decreases in velocity and
436 sub-plate shear lead to a slight increase of mantle viscosity beneath the subducting plate,

compared to the free-sinking stage. After the slab-660 interaction, the viscosity of the sub-plate mantle increases to typically above 10^{20} Pa s.

The slab-660 interaction is followed by two episodes of slab folding. First the slab bends with an OP-wards concavity between ∼6 and ∼14 My (Fig. 6b-c), with an increase in SP velocity (up to 3 cm/yr) and low trench velocity of approximately 1 cm/yr. Then a transient stage of slab rollback, associated with a slight increase in the trench velocities up to 1.5 cm/yr, lasts for approximately 5 My (Fig. 6c) and lowers slab dip in the upper mantle. The second folding episode occurs between ∼25 and ∼40 My: the deeper, folded portion of the slab flattens above the lower mantle while the shallow slab continues to roll back (Fig. 6d), increasing slab pull (v_{sp} up to ~ 2.5 cm/yr). Another transient stage of trench retreat without buckling follows (Fig. 6e), with trench velocity (1.8 cm/yr) greater than the SP velocity (1 cm/yr).

These two folding episodes are reflected in temporal changes in the viscosity of the sub-plate mantle. Its lowest strength is observed during the short SP-velocity peaks, especially underneath the SP (see e.g. Fig. 6c). In contrast, the slight increases in trench/OP motion appear to have little effect on the viscosity field beneath the OP. The highest values of sub-plate mantle viscosity are in fact reached during the stages of slab rollback (Fig. 6e), during which the trench velocity peaks. The sub-plate mantle reaches viscosity values on the order of 10^{21} Pa s, approximately one order of magnitude higher than during SP-velocity peaks.

From 50 My, a third slab-folding episode occurs, but with a smaller amplitude due to the obliquity of slab relative to the viscosity jump (Fig. 6f), and a smaller increase in v_{sp}. Overall, through time, all velocities decrease and tend towards 1 cm/yr, comparable to the sinking velocity of the deepest part of the slab within the lower mantle. Slab sinking rates in the lower mantle therefore strongly modulate, and perhaps even limit, surface kinematics.

The kinematic ratio, K_r, given in Equation 1 provides an alternative quantitative diagnostic. During the free-sinking stage, the slab-tip velocity reaches a peak value of 20 cm/yr, higher than the peak SP velocity v_{sp} (13 cm/yr). As a consequence, the kinematic ratio $K_r \leq 1$ (Fig. 6g). After the slab has interacted with the 660-km discontinuity K_r display oscillations. These oscillation follow those observed for v_{sp} and v_t, when one of the two increases while the other decreases. Folding episodes occur when $K_r >$

1, while slab-retreating stages occurs for lower $K_r \simeq 1$. Through time, the amplitude of K_r oscillations decrease, reflecting the decrease in folding as the slab inclines and the impact angle with the 660-km viscosity discontinuity decreases.

4.1.2 Slab morphologies and kinematic ratios across all standard cases

We run a series of standard simulations with various initial plate ages (20-100 for the overriding plate; 10-100 for the subducting plate). Since we focus on the long-term evolution of these systems (i.e. well after the first stage of slab-free sinking through the upper mantle), Figure 7a only displays their state at $t = 80$ My.

Several studies have focused on the interaction and passage of slabs through the mantle transition and the resulting slab morphologies (Torii & Yoshioka, 2007; Billen, 2010; Lee & King, 2011; Čížková & Bina, 2013; Billen & Arredondo, 2018), sometimes characterizing a range of so-called subduction regimes (Garel et al., 2014; Agrusta et al., 2017; Z.-H. Li et al., 2019; Briaud et al., 2020). Here we focus on two features after initial slab-660 interaction: trench motion and the amount of slab folding. Thus we define three regimes: strong trench retreat without slab folding (SR), strong trench retreat with slab folding (SRwF), and a weak trench retreat with slab folding (WRwF) (7a). The strong-retreat modes are those for which the total displacement of the trench during the simulation amounts to an average rate higher than 1 cm/yr, and weak-retreat modes when it is $\leq$ 1cm/yr. Following, Garel et al. (2014), the results of simulations are reported as functions of initial SP and OP ages, with the former controlling slab buoyancy and resistance to bending, and the latter controlling the OP bending resistance opposing trench retreat. Note that due to our focus on the long-term trench motion and the tendency and nature of slab folding, the subduction regimes outlined herein differ from those used in Garel et al. (2014).

The SR regime in the simulations of the standard case occurs for both relatively old SPs and relatively old OPs. The regime WRwF occurs only for very young SPs. The regime that lies in between, SRwF, occurs over the widest parameter space. In simulations with relatively young OPs, only the SRwF is observed. For extremely young cases ($A_{SP} = A_{OP} = 20$ Myr), subduction is rapidly terminated through slab detachment, because the low slab pull cannot initially overcome the resisting forces.

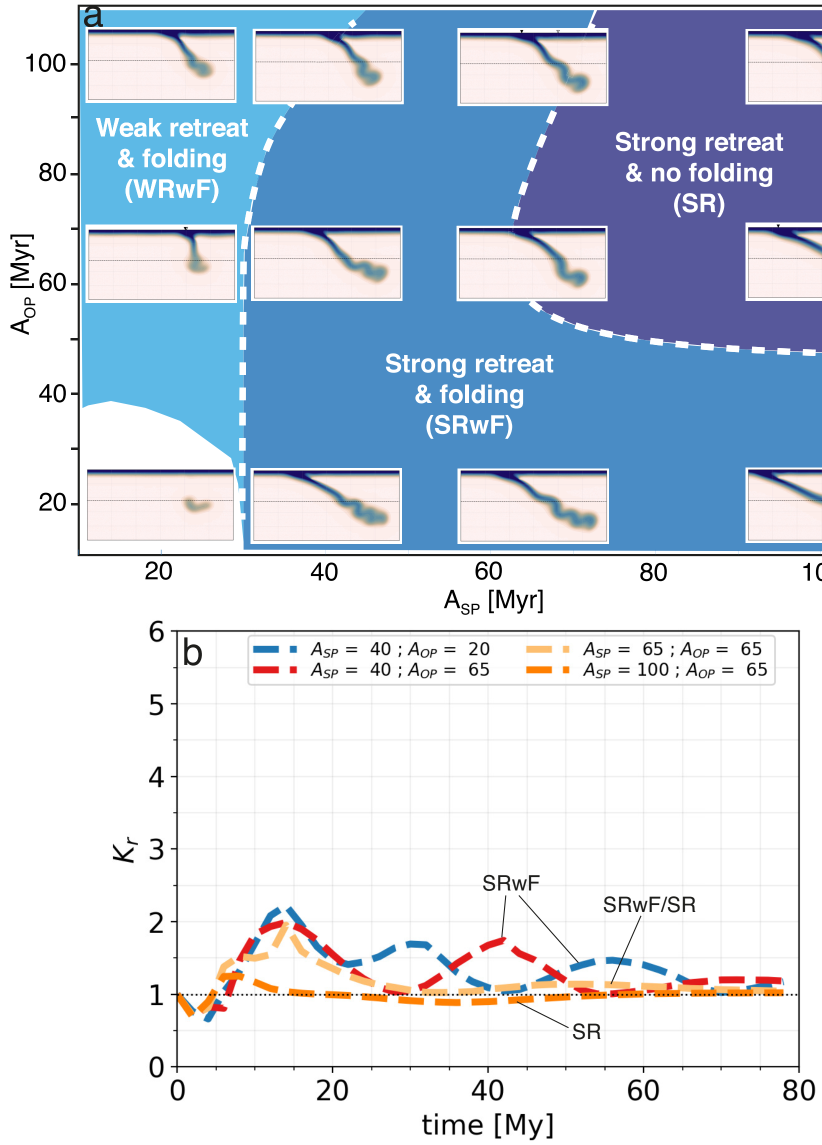

Figure 7. a) Snapshots of the final state (after model run times of 80 My) of all standard models superimposed on a regime diagram. The three regimes are: strong trench retreat without slab folding (SR, purple), strong trench retreat with slab folding (SRwF, dark blue), and weak trench retreat with slab folding (WRwF, light blue). The boundaries between regimes are approximate. b) Kinematic ratio K_r as a function of the time since the initiation of subduction, for four of the standard models shown in (a). The subduction regimes associated with the evolution of those models is indicated by labels. Over time, all four models tend towards no-folding ($K_r \approx 1$).

Figure 7b displays the evolution of K_r for four selected standard simulations. These simulations display peak K_r of 1.5-2.2, shortly after the first slab-660 interaction (time range 5 to 20 Myr). Simulations [A_{sp}=40 My ; A_{op}=20 My] (ref. simulation - SRwF) and [A_{sp}=40 My ; A_{op}=65 My] (SRwF) display oscillations of K_r associated with slab folding. Simulations [A_{sp}=65 My ; A_{op}=65 My] (SR) and [A_{sp}=100 My ; A_{op}=65 My] (SR) display $K_r \sim 1$ at all times after initial slab-660 interaction. At later times, the value of K_r tends to 1, associated a decrease of both v_{sp} and v_s (see Fig. S9 of Supp. Inf.).

4.2 WAL cases

We next perform simulations with a WAL, that is simulations where we impose values of the weakening factor $\alpha < 1$ in the sub-lithospheric mantle. We first consider the a WAL case of moderate weakening of the sub-plate mantle by a factor of two ($\alpha = 0.5$), followed by a more extreme scenario of weakening by a factor of 5 (pronouced WAL case – $\alpha = 0.2$).

4.2.1 Reference simulation of the WAL case

The plate ages are chosen identical to the reference standard case: A_{sp}=40 My and A_{op}=20 My. We apply a two-fold weakening factor ($\alpha = 0.5$). In this simulation reference simulation of the WAL case (Fig. 8), the first slab-660 interaction occurs at ~ 1.5 My, earlier than in the comparable standard simulation ($\simeq$4 My). The first slab buckling episode occurs shortly after, at 2-10 My (Fig. 8a-b), with subducting plate and trench velocities of 5.5 cm/yr and 1 cm/yr, respectively. Compared to the reference standard simulation, the velocities are higher in the WAL simulation during these stages, which likely enhances the strain rate in the sub-plate mantle where the WAL lies. In addition to this intrinsic weakening effect, the lowering of the viscosity by a factor of 0.5 leads to WAL viscosities that can be as low as 10^{19} Pa s even after the first slab-660 interaction.

A second folding episode takes place after 10 My (Fig. 8c-d) during which the SP velocity increases from 1.8 to 3.8 cm/yr between $t = 14$ My and $t = 22$ My and that of the trench decreases from 1.8 to 0.8 cm/yr. The next folding episode (between $t =$ 35 My and $t = 55$ My, Fig. 8e) is associated with a stationary trench, while the SP velocity stabilizes at $\sim$ 2.5 cm/yr. A third fold forms after $t = 55$ My (Fig. 8f), which produces a peak subducting-plate velocity of 4.8 cm/yr. The lowest viscosity of the sub-plate mantle is between 10^{19} and 5×10^{19} Pa s at various stages of the WAL simulation. It never exceeds 10^{20} Pa s, even during stage of slab rollback when SP velocity is typically low (see Supplementary Text S4 and Figure S10 in the Supplementary Info.).

The opposite evolution of trench and SP velocity, associated with K_r oscillation, is even more apparent in the reference WAL simulation than in the reference simulation of the standard case. Since the slab tip velocity remains nearly constant at around 1 cm/yr, independent of slab folding and oscillation of surface velocities, the peaks of K_r in the WAL simulation are due to the peaks in SP velocity which occur simultaneously of the lows in trench motion.

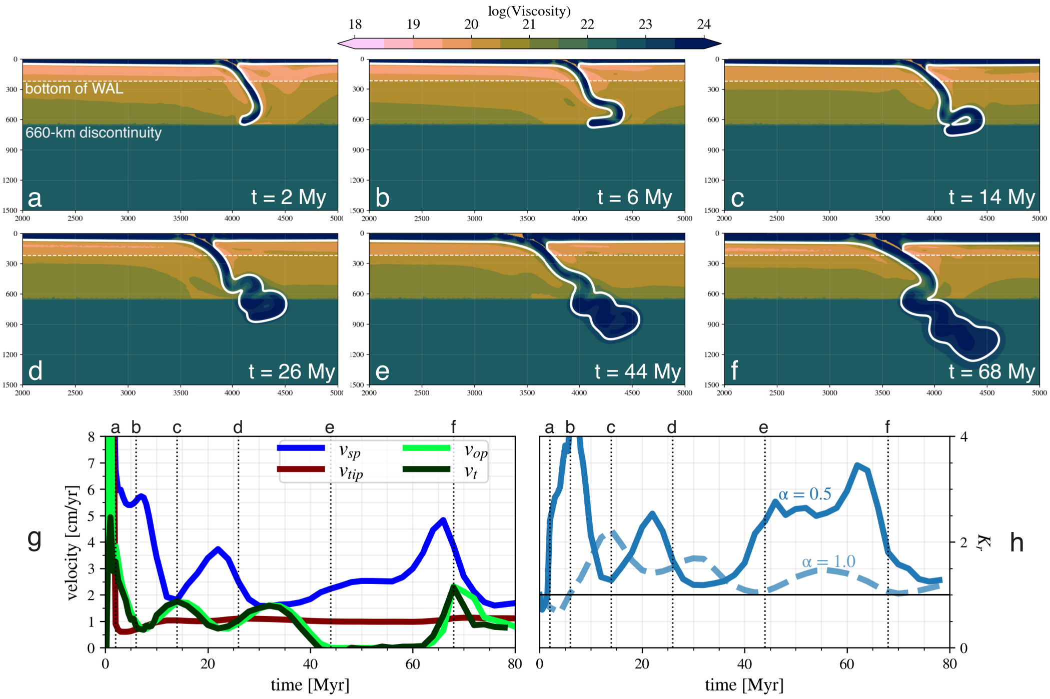

Figure 8. Reference simulation [A_{sp}=40 My ; A_{op}=20My] of the WAL case with a two-fold viscosity reduction ($\alpha = 0.5$). Panels and plotting styles as in Fig. 6. Panel (h) displays the evolution of K_r for this reference WAL case (solid blue) and also for the reference standard case of Fig. 6 (dashed blue).

4.2.2 Mantle drag forces on the subducting plate

At simulation start, the age of the subducting plate at the trench is 40 My in both the reference standard and the reference WAL models. Hence both models feature identical slab pull initially. At simulation end ($t = 80$ My), the SP is 105km thick at the trench (1100°C-isotherm) for the reference WAL case, versus 110km for the reference standard case. Hence the differences in slab pull force in the upper mantle are likely minor in the two simulations. The mid-ocean ridge is free to move over time, and it migrates trenchward by hundreds of kilometers over 80 My runtime, in both models (see Figures S3 and S5). Since the thicknesses and dimensions of the subducting plate remain quite similar in both model cases, the differences in "ridge push force" (driven by potential energy of ridge topography) should be too small to make an appreciable difference in driving plate velocities. Besides, the magnitude of the ridge-push force is estimated about one order of magnitude smaller than that of the slab-pull force (e.g., Forsyth & Uyeda, 1975; Parsons & Richter, 1980; Turcotte & Schubert, 2002).

Hence the divergent evolution of the two reference simulations is most likely explained by a reduction of mantle drag at the base of the subducting plate. We calculate the drag force as the integral of the tangential stress along the 1100°C isotherm (in N m^{-1}). Figure 9 displays the temporal evolution of this diagnostic for the reference simulations (with and without a WAL).

Prior to first slab-660 interaction, both models show sub-lithospheric mantle moving towards the trench, but with velocities reduced relative to the overlying lithosphere (Couette-type flow). Shear stresses beneath the SP are positive and those beneath the OP are mostly negative. Shear stresses along the base of the SP remains positive after slab-660 interaction (Fig. 9c,e), and the drag force remains negative. The absolute value of the drag force beneath the SP decreases with time, as a consequence of the reduction in length of that plate with time.

The two simulations display similar oscillatory trends in SP velocity, which reflect slab folding behavior. The lower absolute drag in the WAL simulation explains its higher SP velocities (Fig. 8g) relative to the comparable non-WAL case (Fig. 6g). A faster SP may hamper trench retreat via faster trench-ward asthenospheric flow, which would oppose to slab rollback (Alsaif et al., 2020). Alternatively, A. F. Holt and Becker (2016) proposed that a reduction in the sub-plate mantle viscosity would decrease the mantle

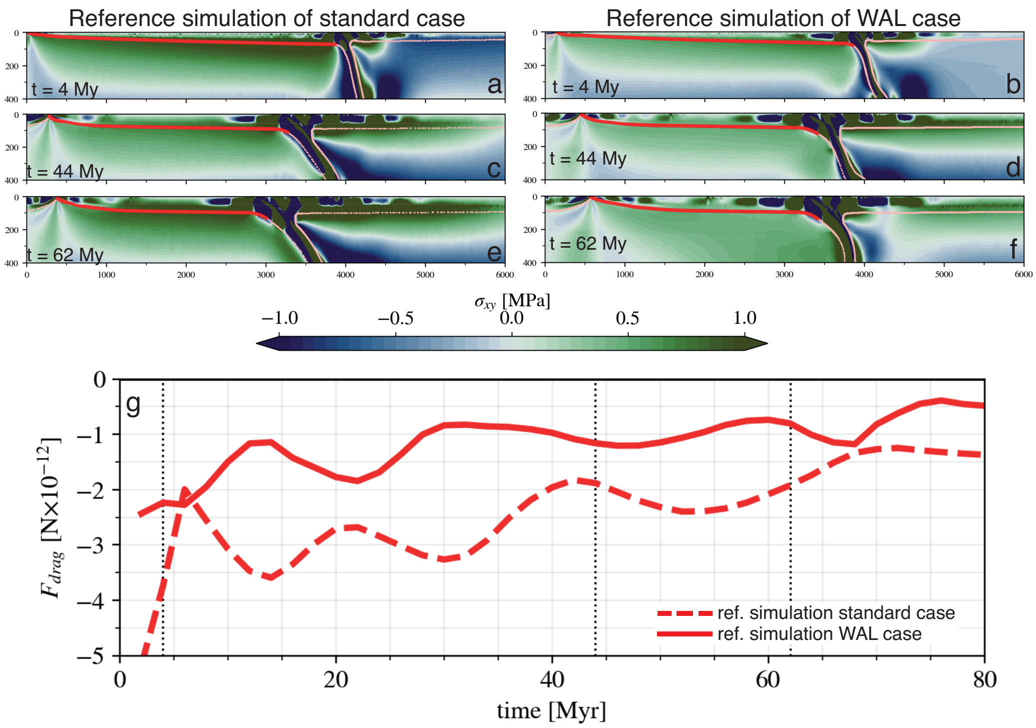

Figure 9. Viscous mantle resistance acting below the subducting plate in the reference standard model versus in the reference WAL model. (a,c,e) Snapshots of the shear stress field (background colour) in the reference standard model at times 4 My, 44 My, and 62 My. (b,d,f) Same snapshots for the reference WAL model. Red line traces the LAB isotherm of 1100°C used to calculate the drag below the subducting plate. Positive shear stresses imply that the tangential component of the stress vector - calculated along the quasi-horizontal LAB isotherm of the subducting plate - is toward the left. g) Evolution of the mantle drag force below the subducting plate for the reference standard model (dashed red) and the reference WAL model (solid red) . Negative values denote a force toward the left. The total mantle drag force onto the subducting plate is negative in accordance with the stress vector. Three vertical dashed lines indicate the times of the snapshopts (a-f). The drag force beneath the overriding plate is less straightforward to analyze, see Supplementary Information Text S5.

drag force acting on the SP to a greater extent than it would decrease the mantle-wedge suction force (Tovish et al., 1978) which opposes to trench motion. As a consequence, these authors suggested that a reduction in sub-plate mantle viscosity would preferentially favor a decrease in trench motion. Finally, a lower drag of the asthenosphere on the subducting slab can also be promoted through the non-newtonian viscosity associated to dislocation creep, causing a positive feedback loop with faster slab inducing larger strain rate and lower viscous resistance to sinking (Garel et al., 2020). All these effects favor the higher K_r observed in the reference WAL case compared to the reference standard case.

We ran a modified reference WAL simulation where the WAL is imposed only beneath the subducting plate ("WAL-SP" model shown in Fig. S12). Its trench displacement and slab morphology are intermediate between the reference WAL and reference standard cases, though tending to a WRwF regime and thus closer overall to the WAL case. This also points to viscosity reduction beneath the SP as the major, causal mechanism for shifting subduction towards a WRwF regime when a WAL is imposed.

4.2.3 Subducting slab morphologies and kinematic ratios in the moderate WAL case ($\alpha = 0.5$)

As with the standard cases, we run a series of WAL simulations with $\alpha = 0.5$, spanning plate ages from 20-100 My. Figure 10a displays their final state at 80 My, together with the inferred regime diagram. Consistent with the standard cases, WAL cases exhibit three regimes (SR, SRwF, and WRwF), but regime boundaries are shifted towards higher plate ages. In particular, the WAL simulations [A_{sp}=65 My-A_{op}=65 My] and [A_{sp}=65 My-A_{op}=100 My] now lie more clearly in the SRwF regime while their standard equivalents belong to the SR regime. Moreover, the WAL simulations with $A_{sp} = 40$ My lie within, or very close to, the WRwF regime, whereas for standard cases, only those with $A_{sp} \geq$ 20 My are within this regime.

Figure 10b displays the kinematic ratio K_r of selected WAL simulations. As in the standard cases, the ratios K_r before and during the first slab-660 interaction is generally higher than 1. Some peak values of K_r reached in the WAL simulations are even greater (> 2) than the highest values observed in the standard simulations (7b). Most importantly, two of these simulations [$A_{sp} = 40$ My;$A_{op} = 20$ My] (ref. simulation for the WAL case) and [$A_{sp} = 65$ My;$A_{op} = 65$ My] display $K_r > 2$ even after the first slab-660 interaction: the presence of a weak layer favors the excess accumulation of subducted material in the mantle relative to the accommodation by motion of both the trench and slab tip, resulting in substantial slab folding. The simulation [A_{sp}=100 My ; A_{op}=65 My] shows values of K_r close to 1 at all times after initial slab-660 interaction, consistent with

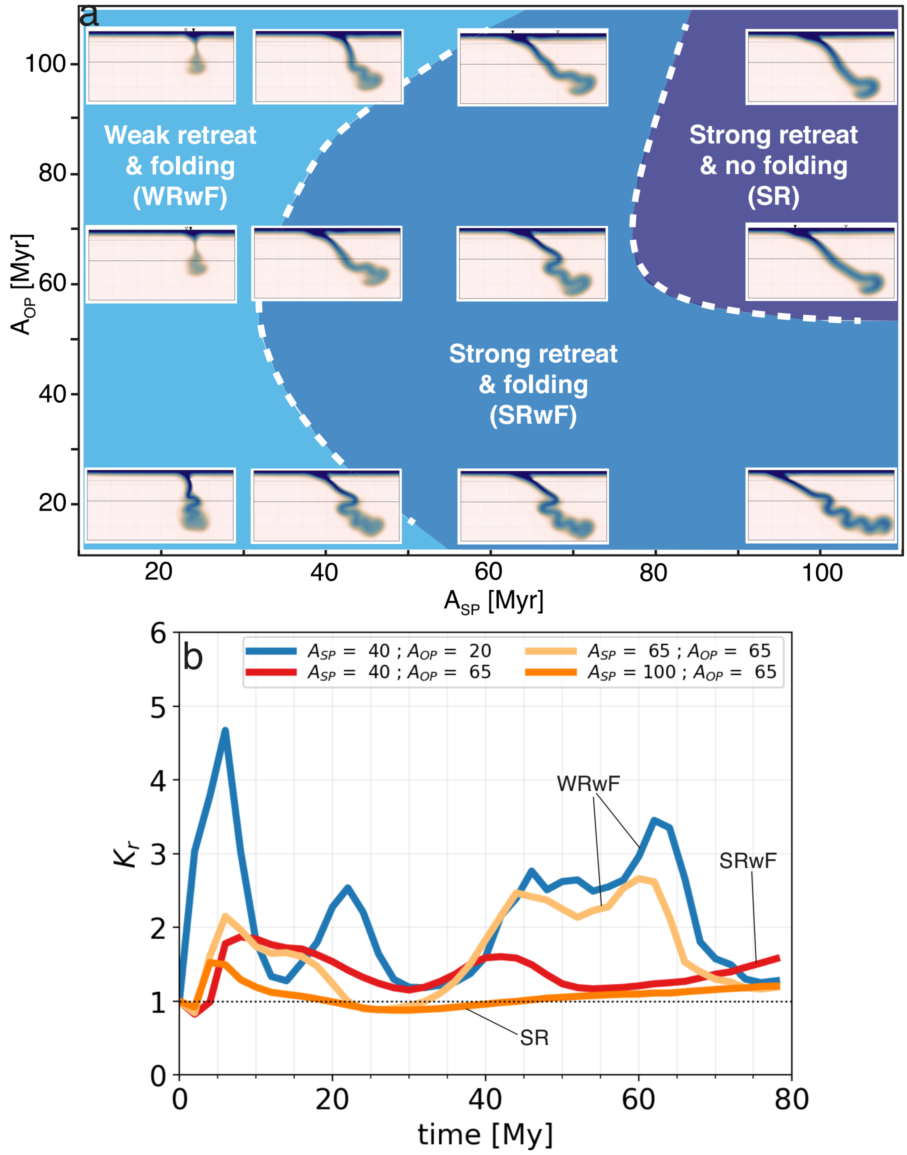

Figure 10. a) Regime diagram of WAL models with two-fold viscosity reduction ($\alpha = 0.5$). Panels and plotting styles as in Fig. 7.

607 the standard case, lying in the SR regime. WAL simulation [A_{sp}=65 My ; A_{op}=65 My]
608 exhibits intermediate behavior, with oscillations of K_r up to 1.5, while its standard equiv-
609 alent show values close to 1. This is because the former clearly lies in the SRwF regime
610 while its equivalent standard case lies near the transition from the SRwF to the SR regime.

4.2.4 Pronounced WAL cases with $\alpha = 0.2$

We finally run a series of simulations for a five-fold weakened WAL with $\alpha = 0.2$ (Fig. 11a). The most striking difference to all previous cases is that the SR regime (strong retreat without folding) no longer appears within the range of plate ages investigated, spanning $A_{sp} = [20\ My, 100\ My]$ and $A_{op} = [20\ My, 100 My]$. Instead, slab folding becomes pervasive throughout the age parameter space. Moreover, the boundary between the WRwF and SRwF regimes shifts to subducting plate ages older than 65 My ,and overriding plate ages older than 20 My. Hence strong trench retreat ($v_t > 1$ cm/yr) now only occurs for dense and stiff subducting plates, with the WRwF regime (folding under quasi-stationary trenches) becoming dominant. In particular, when the overriding plate is weak ($A_{op} \simeq 20$ My), ubiquitously folding slabs pile up almost vertically in the lower mantle. The $\alpha = 0.2$ simulations also sustain higher K_r values (1.5-4) well after the first slab-600 interaction (Fig. 11b).

In most of the pronounced-WAL simulations, soon after the initiation of the model thermal diffusion (cooling from the surface) prevails over advection, and the ridge on the OP side disappears. This enforces a quasi-null trench retreat and enhances vertical folding. As a consequence, the WRwF regime becomes self-sustained from early stages of these simulations.

In most of the pronounced-WAL ($\alpha = 0.2$) simulations, transient thermal instabilities form within the weak layer for simulations with relative old and thick OPs. Drips of cold lithosphere are generated beneath the OP as the lithosphere thicken by conductive cooling. The drips are then advected by lateral mantle flow and mix with the underlying mantle. They only occur when WAL viscosity is close to or below $\sim 10^{19}$ Pa s, consistent with previous studies (van Hunen et al., 2003; Ballmer et al., 2011; Le Voci et al., 2014; D. R. Davies et al., 2016). Finally, simulations run with $\alpha = 0.1$ (not shown) exhibit pronounced thermal instabilities beneath both OP and SP, over a wide range of plate ages (thicknesses). A more detailed analysis of this small-scale convection, however, out of the scope of this study.

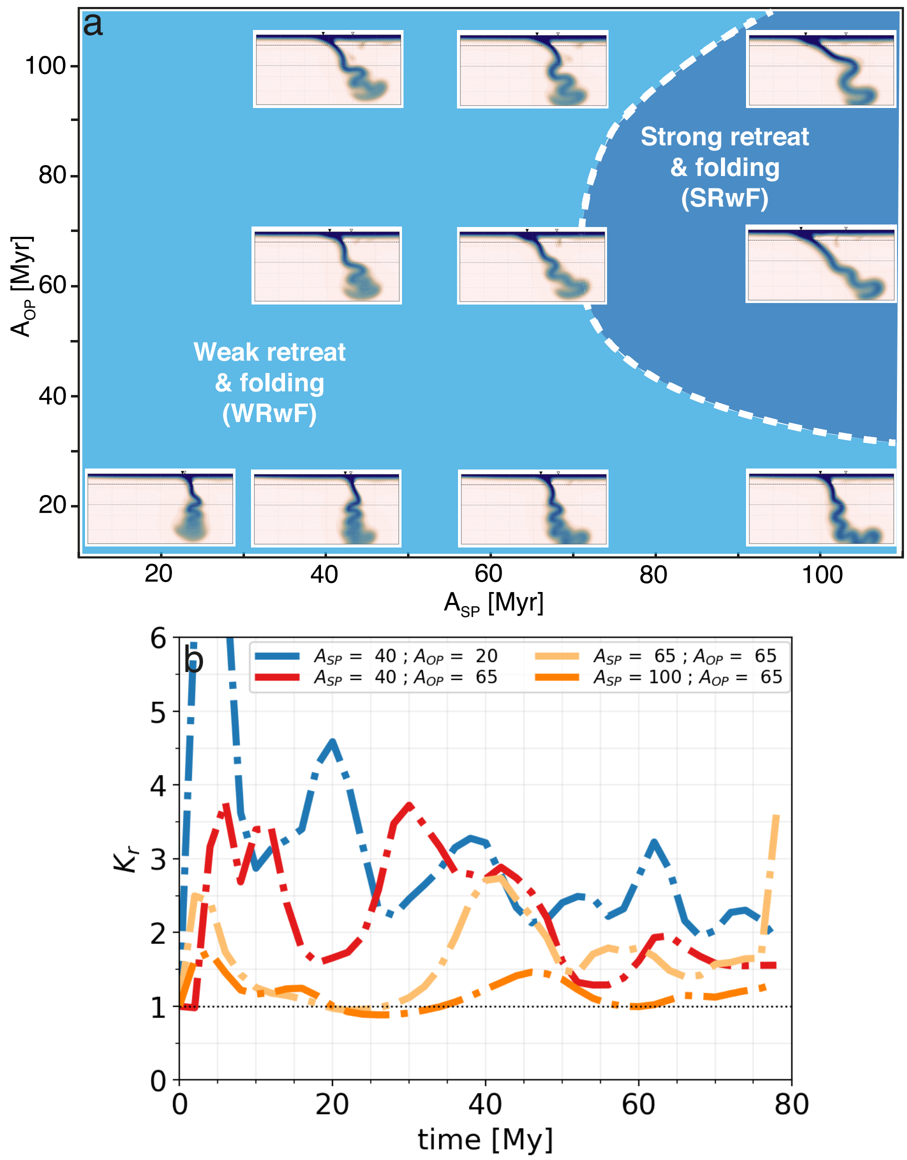

Figure 11. Regime diagram of WAL models with a five-fold viscosity reduction ($\alpha = 0.2$). Panels and plotting styles as in Fig. 7. The models remain in the weak retreat and folding regime over the entire run time, unless they feature very old plate ages.

5 Discussion

5.1 Surface velocities and kinematic ratios

On Earth, subduction rates are typically 3 to 5 times higher than absolute trench velocities, and 5 times higher than estimated slab sinking velocities (see Section 2). This yields kinematic ratio K_r estimates above 1 for most subduction zones, implying that slab thickening/folding is the default regime (see section 2.2).

Simulations without a WAL produce surface kinematics at odds with these observational constraints because once the slab has interacted with the transition zone, the subducting plate v_{sp} slows down to approach slab sinking rates of 1 cm/yr. The addition of a WAL renders the simulations more compatible with observational constraints, in that v_{sp} up to 5 cm/yr are maintained long after initial slab-660 interaction (Fig. S3-S4 in Supp Info), and trench velocities v_t are attenuated to typically lower than 1 cm/yr. Our simulations with WAL thus reproduce the rapid subduction rate, near-stationary trenches, and slow slab-sinking rates observed on Earth. WAL simulations have higher K_r values than the standard models, as summarized by Figure 12. The time-averaged kinematic ratio $\bar{K}_r$ (after initial slab-660 interaction, i.e., averaged between 20-80 My) ranges from 1.0–1.3 in the standard models (Fig. 12a, except for the youngest SP plate ages). In contrast, $\bar{K}_r$ ranges between 1.0–3.1 in the WAL simulations ($\alpha = 0.5$, Fig. 12b), and between 1.0–2.9 for the pronounced-WAL simulations ($\alpha = 0.2$, Fig. 12c). $\bar{K}_r$ is generally higher in the pronounced-WAL simulations (although the maximum value of $\bar{K}_r = 3.1$ occurs for $\alpha = 0.5$ and the youngest plate ages).

Simulations with a WAL also show higher peak values of (non-averaged) K_r, before and after first slab 660-interaction. In the standard models, K_r mostly ranges between 1–2 (see Fig. 7 and Supp Info Fig. S9a), whereas the simulations with a WAL exhibit peak K_r values above 2 and up to 6-7 (Figs. 10 and Fig. 11 – see also Figs. S9b,c in Supp. Info.). Hence only the models with a WAL produce kinematic ratios K_r that are comparable to those estimated for subduction zones in nature (Fig. 4).

Behr and Becker (2018) have suggested the lubrication effect of a weak sedimentary layer above the subducting plate, which gets wedged against the overriding plate at the plate interface, as an alternative mechanism for increasing v_{sp} in models of subduction dynamics (see also Duarte et al., 2013). They showed that v_{sp} could increase by one to two orders of magnitude if sediments reduced viscous resistance at the interface by a comparable amount. Pokorný et al. (2021) demonstrated these possible feedbacks in a subduction system where the weak interface layer has a strain-rate dependent rheology, which may undergo viscosity variations according to the changes in the dynamics of the system. Hence we sought to clarify the role of a weakened plate interface in our own simulations. First we verified that the viscosity of the subduction interface is similar in the WAL and in the standard reference models, at all temporal stages (Fig. S13). This confirms that the very different kinematics of these two models really are due

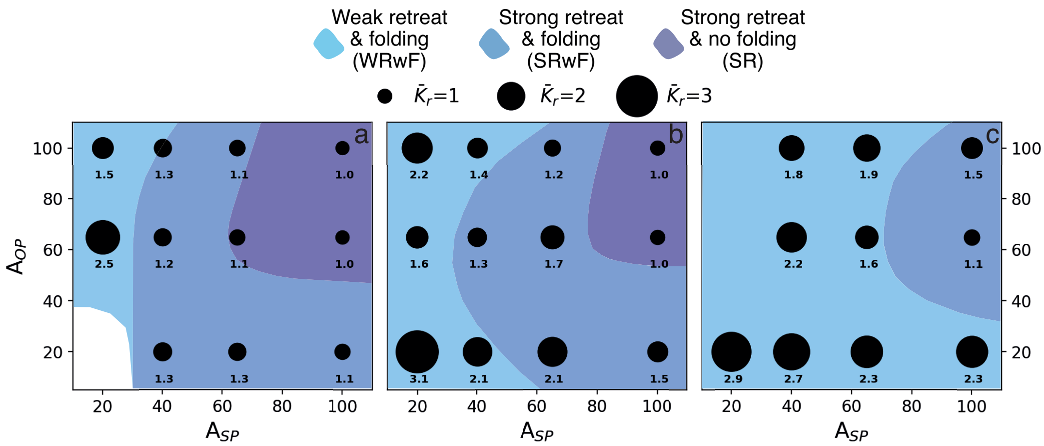

Figure 12. Summary of modeling runs and regime diagrams. Time-averaged kinematic ratio $\bar{K}_r$ after the first slab-600 interaction, plotted in the two-dimensional space of SP and OP plate ages (unit Myr). for (a) standard non-WAL simulations; (b) WAL simulations with $\alpha = 0.5$; (c) pronounced-WAL simulations with $\alpha = 0.2$. $\bar{K}_r$ is represented by black dots with sizes proportional to $\bar{K}_r$ values, which are also printed. Background colors denote folding regimes as in previous figures. The time-averaging window for obtaining $\bar{K}_r$ is [20-80] My.

to the lubrication effect by the WAL, rather than an indirect effect of weaker interface coupling in one model but not the other. Moreover, recent models have shown that a weaker plate interface tends to produce increased trench retreat v_t (Pusok et al., PREPRINT; Behr et al., 2022). We attempted to reproduce this finding by running a standard simulation featuring a plate interface layer with a two-fold reduction in maximum viscosity (see Fig. S8). Relative to the equivalent standard case, v_t did indeed increase slightly, and so did v_{sp}. In combination, K_r hardly changed compared to the standard model, thus remaining too low compared to observations. Hence a weaker plate interface does not narrow the gap between standard model predictions and the available observational constraints and is thus not considered a valid alternative to the WAL hypothesis.

5.2 Slab morphologies

The presence of a WAL strongly impacts the subduction regimes and lower mantle slab morphologies, as encapsulated by the proxy of K_r. Simulations without a WAL produce low-to-moderate values of K_r, and moderate-to-high trench retreat rates. Without a WAL, strong-retreat regimes are thus dominant across the parameter space examined, and only models with the youngest, weakest overriding plate (20 My) exhibit some slab-folding behaviour. In the simulation with a WAL and a weakening factor $\alpha = 0.2$, the (non-folding) SR regime disappears and the SRwF regime only occurs in simulations with relatively stiff and buoyant plates ($A_{sp} > 80$ My,$A_{sp} > 40$ My). Hence, folding slabs and vertically piling in the lower mantle, beneath near-stationary trenches, become the prevailing morphologies when accounting for a WAL in the simulations (light blue shading in Fig.12). These results demonstrate, for the first time, that models of subduction dynamics (without external forcing) are able to produce lower-mantle slab morphologies observed by tomography, while also honouring the plate and trench velocities measured at the surface.

We note that the amplitude of lower-mantle slab folds in our simulations is consistent with theoretical predictions based on a thin-sheet mathematical formulation. Ribe (2003) and Ribe et al. (2007) used these formulations to derive a scaling law for the amplitude of folds of a vertically descending, viscous sheet that buckles as it encounters resistance at a sharp viscosity jump, or a rigid barrier. The predicted fold amplitude is half the fall height, which would be half the thickness of the upper mantle in the context of subduction: approximately 330 km. Our simulations with more pronounced vertical slab folding produce 300 to 500-km wide folds in the lower mantle, that are consistent with this theory. We note that the presence of a WAL enhances the frequency of folding in the models but leaves their width reasonably unchanged. The modeled fold amplitudes of 300-500 km are moderately smaller than the 400-700 km wide “slab walls” imaged by seismic tomography (e. g. Sigloch & Mihalynuk, 2013). It remains to be investigated whether this difference is due to shortcomings of the physical approximations used in our dynamic models, or due to tomographic blur.

From models of subduction dynamics, it has been suggested that sustained, quasi-periodic slab folding, over tens of millions of years after initial slab-660 interaction, can occur only if the mineralogical phase transition around 410 and 660 km were included in the models (Běhounková & Čížková, 2008; Čížková & Bina, 2013; Agrusta et al., 2017; Briaud et al., 2020), and/or if the subducting slab was quite weak, e.g., made of young seafloor (Garel et al., 2014; Agrusta et al., 2017; Strak & Schellart, 2021). While we acknowledge that these factors may further enhance slab folding, we stress that our simulations with a WAL did not require the phase transitions in order to produce sustained slab folding. The Clapeyron slopes of the phase transitions remain under discussion (see e.g. Agrusta et al., 2017, and references therein), so their relative role in slab folding remains to be clarified. In a similar vein, the inclusion of a WAL yielded slab folding of relatively thick and stiff subducting plates (Fig.12). No additional slab-weakening mechanism or slab-buoyancy variation was required. We note that it has also been suggested that vertical piles of lower-mantle slabs are more easily produced in the context of a fixed overriding plate (Lee & King, 2011; Běhounková & Čížková, 2008; Čížková & Bina, 2013; Billen & Arredondo, 2018). Here we have demonstrated that vertical slab folding slab can also occur in simulations with a WAL, in which trench retreat remains self-consistently limited (Fig. 8).

6 Conclusion

Previous numerical and analogue models of subduction dynamics tend to produce surface kinematics and lower-mantle slab morphologies that do not match first-order observational constraints. We have shown that including a weak asthenospheric layer below the lithosphere into numerical models of subduction dynamics eliminates these mismatches. The lubricating effect of the asthenosphere produces a velocity increase of the subducting plate and a reduction of trench retreat, yielding predicted velocities that closely match those recorded on Earth. These velocity changes are sustained long after the subducting slab has penetrated into the lower mantle. The surplus of rapidly subducting lithosphere is accommodated by folding, rather than by accelerating trench retreat or slab sinking. This leads to an apparent horizontal widening of the slab in the lower mantle, as is observed by seismic tomography. Substantial near-vertical slab piles accumulate over time because trench motion is limited. We find that a viscosity reduction below the plate by a factor of only 2 to 5 is sufficient to completely shift the dynamics in these models – from non-folding with slow subduction and substantial trench retreat, to regimes of multiply folded, wall-like slab piles under near-stationary trenches. The latter then dominate across a wide parameter space of subducting and overriding plate ages. Our results provide strong independent support for the presence of a weak asthenospheric layer beneath Earth's lithosphere.

7 Open Research

The data used for Figure 1 and for the estimates of K_r in Fig. 4 is provided in the Supplementary Information Table S1, and is available through the 'SubMAP' website http://submap.gm.univ-montp2.fr/. The tomography model DETOX-P2 used in Fig. 4 is freely available through the 'SubMachine' tomography web portal: http://submachine.earth.ox.ac.uk/. The numerical code, Fluidity, used for the 2-D simulations is open source and available from https://fluidityproject.github.io/. The input files required to reproduce all simulations have been made available in the Zenodo repository https://doi.org/10.5281/zenodo.6817177 which also contains the output files of the reference simulations of both the standard and the WAL cases.

Acknowledgments

N. C. and K.S. were supported by funding to K.S. from the European Research Council (ERC) under the European Union's Horizon 2020 research and innovation program (grant agreement 639003 DEEP TIME). This work was supported by the French government, through the UCAJEDI Investments in the Future project managed by the National Research Agency (ANR) under reference number ANR-15-IDEX-01. The authors are grateful to the OPAL infrastructure from Université Côte d'Azur and the Université Côte d'Azur's Center for High-Performance Computing for providing resources and support.

References

Agrusta, R., Goes, S., & van Hunen, J. (2017). Subducting-slab transition-zone interaction: Stagnation, penetration and mode switches. *Earth and Planetary Science Letters*, *464*, 10–23. Retrieved from `https://doi.org/10.1016/j.epsl.2017.02.005` doi: 10.1016/j.epsl.2017.02.005

Alsaif, M., Garel, F., Gueydan, F., & Davies, D. R. (2020). Upper plate deformation and trench retreat modulated by subduction-driven shallow asthenospheric flows. *Earth and Planetary Science Letters*, *532*, 116013.

Amaru, M. (2007). *Global travel time tomography with 3-d reference models* (Vol. 274). Utrecht University.

Arcay, D., Lallemand, S., & Doin, M.-P. (2008). Back-arc strain in subduction zones: Statistical observations versus numerical modeling. *Geochemistry, Geophysics, Geosystems*, *9*(5).

Argus, D. F., Gordon, R. G., & DeMets, C. (2011). Geologically current motion of 56 plates relative to the no-net-rotation reference frame. *Geochemistry,* *Geophysics, Geosystems*, *12*(11). Retrieved from https://doi.org/10.1029/2011GC003751 doi: 10.1029/2011GC003751

Arredondo, K. M., & Billen, M. I. (2017). Coupled effects of phase transitions and rheology in 2-d dynamical models of subduction. *Journal of Geophysical Research: Solid Earth*, *122*(7), 5813–5830. Retrieved from https://doi.org/10.1002/2017JB014374 doi: 10.1002/2017JB014374

Ballmer, M. D., Ito, G., Van Hunen, J., & Tackley, P. J. (2011). Spatial and temporal variability in hawaiian hotspot volcanism induced by small-scale convection. *Nature Geoscience*, *4*(7), 457–460.

Barruol, G., Sigloch, K., Scholz, J.-R., Mazzullo, A., Stutzmann, E., Montagner, J.-P., ... others (2019). Large-scale flow of indian ocean asthenosphere driven by réunion plume. *Nature Geoscience*, *12*(12), 1043–1049. Retrieved from https://doi.org/10.1038/s41561-019-0479-3 doi: 10.1038/s41561-019-0479-3

Becker, T. W. (2017). Superweak asthenosphere in light of upper mantle seismic anisotropy. *Geochemistry, Geophysics, Geosystems*, *18*(5), 1986–2003. Retrieved from https://doi.org/10.1002/2017GC006886 doi: 10.1002/2017GC006886

Becker, T. W., & Faccenna, C. (2009). A review of the role of subduction dynamics for regional and global plate motions. In *Subduction zone geodynamics* (pp. 3–34). Springer.

Becker, T. W., Schaeffer, A. J., Lebedev, S., & Conrad, C. P. (2015). Toward a generalized plate motion reference frame. *Geophysical Research Letters*, *42*(9), 3188–3196. Retrieved from https://doi.org/10.1002/2015GL063695 doi: 10.1002/2015GL063695

Běhounková, M., & Čížková, H. (2008). Long-wavelength character of subducted slabs in the lower mantle. *Earth and Planetary Science Letters*, *275*(1-2), 43–53. Retrieved from https://doi.org/10.1016/j.epsl.2008.07.059 doi: 10.1016/j.epsl.2008.07.059

Behr, W. M., & Becker, T. W. (2018). Sediment control on subduction plate speeds. *Earth and Planetary Science Letters*, *502*, 166–173. Retrieved from https://doi.org/10.1016/j.epsl.2018.08.057 doi: 10.1016/j.epsl.2018.08.057

Behr, W. M., Holt, A. F., Becker, T. W., & Faccenna, C. (2022). The effects of plate interface rheology on subduction kinematics and dynamics. *Geophysical Journal International*. Retrieved from https://doi.org/10.1093/gji/ggac075 doi: 10.1093/gji/ggac075

Billen, M. I. (2010). Slab dynamics in the transition zone. *Physics of the Earth and planetary interiors*, *183*(1-2), 296–308. Retrieved from https://doi.org/10.1016/j.pepi.2010.05.005 doi: 10.1016/j.pepi.2010.05.005

Billen, M. I., & Arredondo, K. M. (2018). Decoupling of plate-asthenosphere motion caused by non-linear viscosity during slab folding in the transition zone. *Physics of the Earth and Planetary Interiors*, *281*, 17–30. Retrieved from https://doi.org/10.1016/j.pepi.2018.04.011 doi: 10.1016/j.pepi.2018.04.011

Briaud, A., Agrusta, R., Faccenna, C., Funiciello, F., & van Hunen, J. (2020). Topographic fingerprint of deep mantle subduction. *Journal of Geophysical Research: Solid Earth*, *125*(1), e2019JB017962. Retrieved from https://doi.org/10.1029/2019JB017962 doi: 10.1029/2019JB017962

Butterworth, N., Talsma, A., Müller, R., Seton, M., Bunge, H.-P., Schuberth, B., … Heine, C. (2014). Geological, tomographic, kinematic and geodynamic constraints on the dynamics of sinking slabs. *Journal of Geodynamics*, *73*, 1–13. Retrieved from https://doi.org/10.1016/j.jog.2013.10.006 doi: 10.1016/j.jog.2013.10.006

Čadek, O., & Fleitout, L. (1999). A global geoid model with imposed plate velocities and partial layering. *Journal of Geophysical Research: Solid Earth*, *104*(B12), 29055–29075. Retrieved from https://doi.org/10.1029/1999JB900150 doi: 10.1029/1999JB900150

Capitanio, F., Morra, G., & Goes, S. (2007). Dynamic models of downgoing plate-buoyancy driven subduction: Subduction motions and energy dissipation. *Earth and Planetary Science Letters*, *262*(1), 284–297. doi: 10.1016/j.epsl.2007.07.039

Carluccio, R., Kaus, B., Capitanio, F. A., & Moresi, L. (2019). The impact of a very weak and thin upper asthenosphere on subduction motions. *Geophysical Research Letters*, *46*(21), 11893–11905. Retrieved from https://doi.org/10.1029/2019GL085212 doi: 10.1029/2019GL085212

Cerpa, N. G., Araya, R., Gerbault, M., & Hassani, R. (2015). Relationship between slab dip and topography segmentation in an oblique subduction zone: Insights from numerical modeling. *Geophysical Research Letters*, *42*(14), 5786–5795. doi: 10.1002/2015GL064047

Cerpa, N. G., Guillaume, B., & Martinod, J. (2018). The interplay between overriding plate kinematics, slab dip and tectonics. *Geophysical Journal International*, *215*(3), 1789-1802. doi: 10.1093/gji/ggy365

Cerpa, N. G., Hassani, R., Gerbault, M., & Prévost, J.-H. (2014). A fictitious domain method for lithosphere-asthenosphere interaction: Application to periodic slab folding in the upper mantle. *Geochemistry, Geophysics, Geosystems*, *15*(5), 1852–1877. Retrieved from `https://doi.org/10.1002/2014GC005241` doi: 10.1002/2014GC005241

Chantel, J., Manthilake, G., Andrault, D., Novella, D., Yu, T., & Wang, Y. (2016). Experimental evidence supports mantle partial melting in the asthenosphere. *Science advances*, *2*(5), e1600246. Retrieved from `https://doi.org/10.1126/sciadv.1600246`

Christensen, U. R. (1996). The influence of trench migration on slab penetration into the lower mantle. *Earth and Planetary Science Letters*, *140*(1), 27–39. doi: 10.1016/0012-821X(96)00023-4

Čížková, H., & Bina, C. (2013). Effects of mantle and subduction-interface rheologies on slab stagnation and trench rollback. *Earth and Planetary Science Letters*, *379*, 95–103. doi: 10.1016/j.epsl.2013.08.011

Čížková, H., & Bina, C. R. (2015). Geodynamics of trench advance: Insights from a philippine-sea-style geometry. *Earth and Planetary Science Letters*, *430*, 408–415. Retrieved from `https://doi.org/10.1016/j.epsl.2015.07.004` doi: 10.1016/j.epsl.2015.07.004

Čížková, H., van den Berg, A. P., Spakman, W., & Matyska, C. (2012). The viscosity of earth's lower mantle inferred from sinking speed of subducted lithosphere. *Physics of the earth and Planetary Interiors*, *200*, 56–62. Retrieved from `https://doi.org/10.1016/j.pepi.2012.02.010` doi: 10.1016/j.pepi.2012.02.010

Coltice, N., Rolf, T., Tackley, P. J., & Labrosse, S. (2012). Dynamic causes of the relation between area and age of the ocean floor. *Science*, *336*(6079), 335–338. Retrieved from `https://doi.org/10.1126/science.1219120` doi: 10.1126/

science.1219120

Conrad, C. P., & Behn, M. D. (2010). Constraints on lithosphere net rotation and asthenospheric viscosity from global mantle flow models and seismic anisotropy. *Geochemistry, Geophysics, Geosystems*, *11*(5). Retrieved from https://doi.org/10.1029/2009GC002970 doi: 10.1029/2009GC002970

Cooper, R., & Kohlstedt, D. (1986). Rheology and structure of olivine-basalt partial melts. *Journal of Geophysical Research: Solid Earth*, *91*(B9), 9315–9323. Retrieved from https://doi.org/10.1029/JB091iB09p09315 doi: 10.1029/JB091iB09p09315

Davies, D. R., Le Voci, G., Goes, S., Kramer, S. C., & Wilson, C. R. (2016). The mantle wedge's transient 3-D flow regime and thermal structure. *Geochem. Geophys. Geosys.*, *17*, 78-100. doi: 10.1002/2015GC006125

Davies, D. R., Wilson, C., & Kramer, S. (2011). Fluidity: A fully unstructured anisotropic adaptive mesh computational modeling framework for geodynamics. *Geochemistry, Geophysics, Geosystems*, *12*(6). Retrieved from https://doi.org/10.1029/2011GC003551 doi: 10.1029/2011GC003551

Davies, G. (1981). Regional compensation of subducted lithosphere: effects on geoid, gravity and topography from a preliminary model. *Earth and Planetary Science Letters*, *54*(3), 431–441. Retrieved from https://doi.org/10.1016/0012-821X(81)90059-5 doi: 10.1016/0012-821X(81)90059-5

Debayle, E., Bodin, T., Durand, S., & Ricard, Y. (2020). Seismic evidence for partial melt below tectonic plates. *Nature*, *586*(7830), 555–559. Retrieved from https://doi.org/10.1038/s41586-020-2809-4 doi: 10.1038/s41586-020-2809-4

Debayle, E., & Ricard, Y. (2013). Seismic observations of large-scale deformation at the bottom of fast-moving plates. *Earth and Planetary Science Letters*, *376*, 165–177. Retrieved from https://doi.org/10.1016/j.epsl.2013.06.025 doi: 10.1016/j.epsl.2013.06.025

Di Giuseppe, E., Van Hunen, J., Funiciello, F., Faccenna, C., & Giardini, D. (2008). Slab stiffness control of trench motion: Insights from numerical models. *Geochemistry, Geophysics, Geosystems*, *9*(2).

Doglioni, C., Carminati, E., Cuffaro, M., & Scrocca, D. (2007). Subduction kinematics and dynamic constraints. *Earth-Science Reviews*, *83*(3), 125–175.

Domeier, M., Doubrovine, P. V., Torsvik, T. H., Spakman, W., & Bull, A. L. (2016). Global correlation of lower mantle structure and past subduction. *Geophysical Research Letters*, *43*(10), 4945–4953. Retrieved from https://doi.org/10.1002/2016GL068827 doi: 10.1002/2016GL068827

Doubrovine, P. V., Steinberger, B., & Torsvik, T. H. (2012). Absolute plate motions in a reference frame defined by moving hot spots in the pacific, atlantic, and indian oceans. *Journal of Geophysical Research: Solid Earth*, *117*(B9). Retrieved from https://doi.org/10.1029/2011JB009072 doi: 10.1029/2011JB009072

Duarte, J. C., Schellart, W. P., & Cruden, A. R. (2013). Three-dimensional dynamic laboratory models of subduction with an overriding plate and variable interplate rheology. *Geophysical Journal International*, ggt257.

Forsyth, D., & Uyeda, S. (1975). On the relative importance of the driving forces of plate motion. *Geophysical Journal International*, *43*(1), 163–200.

French, S., Lekic, V., & Romanowicz, B. (2013). Waveform tomography reveals channeled flow at the base of the oceanic asthenosphere. *Science*, *342*(6155), 227–230. Retrieved from https://doi.org/10.1126/science.1241514 doi: 10.1126/science.1241514

Fukao, Y., & Obayashi, M. (2013). Subducted slabs stagnant above, penetrating through, and trapped below the 660 km discontinuity. *Journal of Geophysical Research: Solid Earth*, *118*(11), 5920–5938. doi: 10.1002/2013JB010466

Fukao, Y., Obayashi, M., Inoue, H., & Nenbai, M. (1992). Subducting slabs stagnant in the mantle transition zone. *Journal of Geophysical Research: Solid Earth (1978–2012)*, *97*(B4), 4809–4822.

Funiciello, F., Faccenna, C., & Giardini, D. (2004). Role of lateral mantle flow in the evolution of subduction systems: insights from laboratory experiments. *Geophysical Journal International*, *157*(3), 1393–1406. doi: 10.1111/j.1365-246X.2004.02313.x

Funiciello, F., Faccenna, C., Heuret, A., Lallemand, S., Di Giuseppe, E., & Becker, T. (2008). Trench migration, net rotation and slab–mantle coupling. *Earth and Planetary Science Letters*, *271*(1), 233–240. doi: 10.1016/j.epsl.2008.04.006

Garel, F., Goes, S., Davies, D. R., Davies, J., Kramer, S., & Wilson, C. (2014). Interaction of subducted slabs with the mantle transition-zone: A regime diagram from 2-d thermo-mechanical models with a mobile trench and an overriding plate. *Geochemistry, Geophysics, Geosystems*. Retrieved from https://doi.org/10.1002/2014GC005257 doi: 10.1002/2014GC005257

Garel, F., Thoraval, C., Tommasi, A., Demouchy, S., & Davies, D. R. (2020). Using thermo-mechanical models of subduction to constrain effective mantle viscosity. *Earth and Planetary Science Letters*, *539*, 116243.

Gibert, G., Gerbault, M., Hassani, R., & Tric, E. (2012). Dependency of slab geometry on absolute velocities and conditions for cyclicity: insights from numerical modelling. *Geophysical Journal International*, *189*(2), 747–760. Retrieved 2013-12-05, from https://doi.org/10.1111/j.1365-246X.2012.05426.x doi: 10.1111/j.1365-246X.2012.05426.x

Goes, S., Agrusta, R., Van Hunen, J., & Garel, F. (2017). Subduction-transition zone interaction: A review. *Geosphere*, *13*(3), 644–664. Retrieved from https://doi.org/10.1130/GES01476.1 doi: 10.1130/GES01476.1

Goes, S., Capitanio, F. A., Morra, G., Seton, M., & Giardini, D. (2011). Signatures of downgoing plate-buoyancy driven subduction in cenozoic plate motions. *Physics of the Earth and Planetary Interiors*, *184*(1), 1–13. Retrieved from https://doi.org/10.1016/j.pepi.2010.10.007 doi: 10.1016/j.pepi.2010.10.007

Guillaume, B., Hertgen, S., Martinod, J., & Cerpa, N. (2018). Slab dip, surface tectonics: How and when do they change following an acceleration/slow down of the overriding plate? *Tectonophysics*, *726*, 110–120. doi: 10.1016/j.tecto.2018.01.030

Guillou-Frottier, L., Buttles, J., & Olson, P. (1995). Laboratory experiments on the structure of subducted lithosphere. *Earth and Planetary Science Letters*, *133*(1), 19–34.

Gurnis, M. (1993). Phanerozoic marine inundation of continents driven by dynamic topography above subducting slabs. *Nature*, *364*(6438), 589–593. Retrieved from https://doi.org/10.1038/364589a0 doi: 10.1038/364589a0

Gurnis, M., & Hager, B. H. (1988). Controls of the structure of subducted slabs. *Nature*, *335*(6188), 317–321. Retrieved from https://doi.org/10.1038/335317a0 doi: 10.1038/335317a0

Hager, B., & Richards, M. (1989). Long-wavelength variations in earth's geoid:

physical models and dynamical implications. *Philosophical Transactions of the Royal Society of London. Series A, Mathematical and Physical Sciences*, *328*(1599), 309–327. Retrieved from https://doi.org/10.1098/rsta.1989.0038 doi: 10.1098/rsta.1989.0038

Hager, B. H. (1984). Subducted slabs and the geoid: Constraints on mantle rheology and flow. *Journal of Geophysical Research: Solid Earth*, *89*(B7), 6003–6015. Retrieved from https://doi.org/10.1029/JB089iB07p06003 doi: 10.1029/JB089iB07p06003

Hertgen, S., Yamato, P., Guillaume, B., Magni, V., Schliffke, N., & van Hunen, J. (2020). Influence of the thickness of the overriding plate on convergence zone dynamics. *Geochemistry, Geophysics, Geosystems*, *21*(2), e2019GC008678. Retrieved from https://doi.org/10.1029/2019GC008678 doi: 10.1029/2019GC008678

Heuret, A., Funiciello, F., Faccenna, C., & Lallemand, S. (2007). Plate kinematics, slab shape and back-arc stress: a comparison between laboratory models and current subduction zones. *Earth and Planetary Science Letters*, *256*(3), 473–483. doi: 10.1016/j.epsl.2007.02.004

Heuret, A., & Lallemand, S. (2005). Plate motions, slab dynamics and back-arc deformation. *Physics of the Earth and Planetary Interiors*, *149*(1), 31–51. doi: 10.1016/j.pepi.2004.08.022

Höink, T., Lenardic, A., & Richards, M. (2012). Depth-dependent viscosity and mantle stress amplification: implications for the role of the asthenosphere in maintaining plate tectonics. *Geophysical Journal International*, *191*(1), 30–41. Retrieved from https://doi.org/10.1111/j.1365-246X.2012.05621.x doi: 10.1111/j.1365-246X.2012.05621.x

Holt, A., Becker, T., & Buffett, B. (2015). Trench migration and overriding plate stress in dynamic subduction models. *Geophysical Journal International*, *201*(1), 172–192. Retrieved from https://doi.org/10.1093/gji/ggv011 doi: 10.1093/gji/ggv011

Holt, A. F., & Becker, T. W. (2016). The effect of a power-law mantle viscosity on trench retreat rate. *Geophysical Journal International*, ggw392. Retrieved from https://doi.org/10.1093/gji/ggw392 doi: 10.1093/gji/ggw392

Holtzman, B. K. (2016). Questions on the existence, persistence, and mechanical effects of a very small melt fraction in the asthenosphere. *Geochemistry, Geophysics, Geosystems*, *17*(2), 470–484. Retrieved from https://doi.org/10.1002/2015GC006102 doi: 10.1002/2015GC006102

Hosseini, K., Sigloch, K., Tsekhmistrenko, M., Zaheri, A., Nissen-Meyer, T., & Igel, H. (2020). Global mantle structure from multifrequency tomography using p, pp and p-diffracted waves. *Geophysical Journal International*, *220*(1), 96–141. Retrieved from https://doi.org/10.1093/gji/ggz394 doi: 10.1093/gji/ggz394

Jarrard, R. D. (1986). Relations among subduction parameters. *Reviews of Geophysics*, *24*(2), 217–284. doi: 10.1029/RG024i002p00217

Jones, T., Davies, D., Campbell, I., Wilson, C., & Kramer, S. (2016). Do mantle plumes preserve the heterogeneous structure of their deep-mantle source? *Earth Planet. Sci. Lett.*, *434*, 10 - 17. doi: 10.1016/j.epsl.2015.11.016

Karason, H., & Van Der Hilst, R. D. (2000). Constraints on mantle convection from seismic tomography. *The History and Dynamics of Global Plate Motions*, 277–288.

Kawakatsu, H., Kumar, P., Takei, Y., Shinohara, M., Kanazawa, T., Araki, E., & Suyehiro, K. (2009). Seismic evidence for sharp lithosphere-asthenosphere boundaries of oceanic plates. *science*, *324*(5926), 499–502. Retrieved from https://doi.org/10.1126/science.1169499 doi: 10.1126/science.1169499

Kohlstedt, D. L., & Zimmerman, M. E. (1996). Rheology of partially molten mantle rocks. *Annual Review of Earth and Planetary Sciences*, *24*(1), 41–62. Retrieved from https://doi.org/10.1146/annurev.earth.24.1.41 doi: 10.1146/annurev.earth.24.1.41

Kramer, S., Wilson, C., & Davies, D. R. (2012). An implicit free surface algorithm for geodynamical simulations. *Physics of the Earth and Planetary Interiors*, *194*, 25–37. Retrieved from https://doi.org/10.1016/j.pepi.2012.01.001 doi: 10.1016/j.pepi.2012.01.001

Kramer, S. C., Davies, D. R., & Wilson, C. R. (2021). Analytical solutions for mantle flow in cylindrical and spherical shells. *Geosci. Model Dev.*, *14*, 1899–1919. doi: 10.5194/gmd-14-1899-2021

Lallemand, S., Heuret, A., & Boutelier, D. (2005). On the relationships between slab dip, back-arc stress, upper plate absolute motion, and crustal nature in subduction zones. *Geochemistry, Geophysics, Geosystems*, *6*(9). doi: 10.1029/2005GC000917

Lee, C., & King, S. D. (2011). Dynamic buckling of subducting slabs reconciles geological and geophysical observations. *Earth and Planetary Science Letters*, *312*(3), 360–370.

Lenardic, A., Richards, M., & Busse, F. H. (2006). Depth-dependent rheology and the horizontal length scale of mantle convection. *Journal of Geophysical Research: Solid Earth*, *111*(B7).

Le Voci, G., Davies, D. R., Goes, S., Kramer, S. C., & Wilson, C. R. (2014). A systematic 2-D investigation into the mantle wedge's transient flow regime and thermal structure: complexities arising from a hydrated rheology and thermal buoyancy. *Geochem. Geophys. Geosys.*, *15*, 28–51. doi: 10.1002/2013GC005022

Li, C., van der Hilst, R. D., Engdahl, E. R., & Burdick, S. (2008). A new global model for p wave speed variations in earth's mantle. *Geochemistry, Geophysics, Geosystems*, *9*(5).

Li, Z.-H., Gerya, T., & Connolly, J. A. (2019). Variability of subducting slab morphologies in the mantle transition zone: Insight from petrological-thermomechanical modeling. *Earth-Science Reviews*, *196*, 102874. Retrieved from https://doi.org/10.1016/j.earscirev.2019.05.018 doi: 10.1016/j.earscirev.2019.05.018

Loiselet, C., Braun, J., Husson, L., Le Carlier de Veslud, C., Thieulot, C., Yamato, P., & Grujic, D. (2010). Subducting slabs: Jellyfishes in the earth's mantle. *Geochemistry, Geophysics, Geosystems*, *11*(8). Retrieved from https://doi.org/10.1029/2010GC003172 doi: 10.1029/2010GC003172

Lyu, T., Zhu, Z., & Wu, B. (2019). Subducting slab morphology and mantle transition zone upwelling in double-slab subduction models with inward-dipping directions. *Geophysical Journal International*, *218*(3), 2089–2105. Retrieved from https://doi.org/10.1093/gji/ggz268 doi: 10.1093/gji/ggz268

Meyers, C. D., & Kohlstedt, D. L. (2021). Experimental measurements of anisotropic viscosity in naturally sourced dunite with a preexisting cpo. *Tectonophysics*, *815*, 228949. Retrieved from https://doi.org/10.1016/j.tecto.2021.228949 doi: 10.1016/j.tecto.2021.228949

Mitrovica, J., & Forte, A. (2004). A new inference of mantle viscosity based upon joint inversion of convection and glacial isostatic adjustment data. *Earth and Planetary Science Letters*, *225*(1), 177–189. doi: 10.1016/j.epsl.2004.06.005

Mohammadzaheri, A., Sigloch, K., Hosseini, K., & Mihalynuk, M. G. (2021). Subducted lithosphere under south america from multi-frequency p-wave tomography. *Journal of Geophysical Research: Solid Earth*, *126*, e2020JB020704. Retrieved from `https://doi.org/10.1029/2020JB020704` doi: 10.1029/2020JB020704

Montagner, J.-P., & Tanimoto, T. (1991). Global upper mantle tomography of seismic velocities and anisotropies. *Journal of Geophysical Research: Solid Earth*, *96*(B12), 20337–20351. Retrieved from `https://doi.org/10.1029/91JB01890` doi: 10.1029/91JB01890

Naif, S., Key, K., Constable, S., & Evans, R. (2013). Melt-rich channel observed at the lithosphere–asthenosphere boundary. *Nature*, *495*(7441), 356–359. Retrieved from `https://doi.org/10.1038/nature11939` doi: 10.1038/nature11939

Parsons, B., & Richter, F. (1980). A relation between the driving force and geoid anomaly associated with mid-ocean ridges. *Earth and Planetary Science Letters*, *51*(2), 445–450.

Paulson, A., & Richards, M. A. (2009). On the resolution of radial viscosity structure in modelling long-wavelength postglacial rebound data. *Geophysical Journal International*, *179*(3), 1516–1526. Retrieved from `https://doi.org/10.1111/j.1365-246X.2009.04362.x` doi: 10.1111/j.1365-246X.2009.04362.x

Phipps Morgan, J., Morgan, W. J., Zhang, Y.-S., & Smith, W. H. (1995). Observational hints for a plume-fed, suboceanic asthenosphere and its role in mantle convection. *Journal of Geophysical Research: Solid Earth*, *100*(B7), 12753–12767. Retrieved from `https://doi.org/10.1029/95JB00041` doi: 10.1029/95JB00041

Pokornỳ, J., Čížková, H., & van den Berg, A. (2021). Feedbacks between subduction dynamics and slab deformation: Combined effects of nonlinear rheology of a weak decoupling layer and phase transitions. *Physics of the Earth and Planetary Interiors*, *313*, 106679. Retrieved from `https://doi.org/10.1016/j.pepi.2021.106679` doi: 10.1016/j.pepi.2021.106679

Pusok, A. E., Stegman, D. R., & Kerr, M. (PREPRINT). The effect of sediments on the dynamics and accretionary style of subduction margins. *Solid Earth Discussions*, 1–30.

Raterron, P., Chen, J., Geenen, T., & Girard, J. (2011). Pressure effect on forsterite dislocation slip systems: Implications for upper-mantle lpo and low viscosity zone. *Physics of the Earth and Planetary Interiors*, *188*(1-2), 26–36.

Ren, Y., Stutzmann, E., van Der Hilst, R. D., & Besse, J. (2007). Understanding seismic heterogeneities in the lower mantle beneath the americas from seismic tomography and plate tectonic history. *Journal of Geophysical Research: Solid Earth*, *112*(B1). Retrieved from https://doi.org/10.1029/2005JB004154 doi: 10.1029/2005JB004154

Ribe, N. M. (2003). Periodic folding of viscous sheets. *Physical Review E*, *68*(3), 036305. doi: 10.1103/PhysRevE.68.036305

Ribe, N. M. (2010). Bending mechanics and mode selection in free subduction: a thin-sheet analysis. *Geophysical Journal International*, *180*(2), 559–576. Retrieved from https://doi.org/10.1111/j.1365-246X.2009.04460.x doi: 10.1111/j.1365-246X.2009.04460.x

Ribe, N. M., Stutzmann, E., Ren, Y., & Van Der Hilst, R. (2007). Buckling instabilities of subducted lithosphere beneath the transition zone. *Earth and Planetary Science Letters*, *254*(1), 173–179.

Ricard, Y., Doglioni, C., & Sabadini, R. (1991). Differential rotation between lithosphere and mantle: a consequence of lateral mantle viscosity variations. *Journal of Geophysical Research: Solid Earth*, *96*(B5), 8407–8415. Retrieved from https://doi.org/10.1029/91JB00204 doi: 10.1029/91JB00204

Ricard, Y., Richards, M., Lithgow-Bertelloni, C., & Le Stunff, Y. (1993). A geodynamic model of mantle density heterogeneity. *Journal of Geophysical Research: Solid Earth*, *98*(B12), 21895–21909. Retrieved from https://doi.org/10.1029/93JB02216 doi: 10.1029/93JB02216

Richards, M. A. (1991). Hotspots and the case for a high viscosity lower mantle. In *Glacial isostasy, sea-level and mantle rheology* (pp. 571–587). Springer. Retrieved from https://doi.org/10.1007/978-94-011-3374-6_27 doi: 10.1007/978-94-011-3374-6_27

Sakamaki, T., Suzuki, A., Ohtani, E., Terasaki, H., Urakawa, S., Katayama, Y., . . .

Ballmer, M. D. (2013). Ponded melt at the boundary between the lithosphere and asthenosphere. *Nature Geoscience*, *6*(12), 1041–1044. Retrieved from https://doi.org/10.1038/ngeo1982 doi: 10.1038/ngeo1982

Schellart, W. P. (2005). Influence of the subducting plate velocity on the geometry of the slab and migration of the subduction hinge. *Earth and Planetary Science Letters*, *231*(3-4), 197–219. Retrieved from https://doi.org/10.1016/j.epsl.2004.12.019 doi: 10.1016/j.epsl.2004.12.019

Schellart, W. P. (2008a). Kinematics and flow patterns in deep mantle and upper mantle subduction models: Influence of the mantle depth and slab to mantle viscosity ratio. *Geochemistry, Geophysics, Geosystems*, *9*(3). Retrieved from https://doi.org/10.1111/10.1029/2004JB002970 doi: 10.1029/2004JB002970

Schellart, W. P. (2008b). Subduction zone trench migration: Slab driven or overriding-plate-driven? *Physics of the Earth and Planetary Interiors*, *170*(1-2), 73–88. Retrieved from https://doi.org/10.1016/j.pepi.2008.07.040 doi: 10.1016/j.pepi.2008.07.040

Schmerr, N. (2012). The gutenberg discontinuity: Melt at the lithosphere-asthenosphere boundary. *Science*, *335*(6075), 1480–1483. Retrieved from https://doi.org/10.1126/science.1215433 doi: 10.1126/science.1215433

Sdrolias, M., & Müller, R. (2006). Controls on back-arc basin formation. *Geochemistry, Geophysics, Geosystems*, *7*(4). doi: 10.1029/2005GC001090

Sharples, W., Jadamec, M., Moresi, L., & Capitanio, F. (2014). Overriding plate controls on subduction evolution. *Journal of Geophysical Research: Solid Earth*, *119*(8), 6684–6704. Retrieved from https://doi.org/10.1002/2014JB011163 doi: 10.1002/2014JB011163

Shephard, G. E., Matthews, K. J., Hosseini, K., & Domeier, M. (2017). On the consistency of seismically imaged lower mantle slabs. *Scientific reports*, *7*(1), 1–17. Retrieved from https://doi.org/10.1038/s41598-017-11039-w doi: 10.1038/s41598-017-11039-w

Sigloch, K., McQuarrie, N., & Nolet, G. (2008). Two-stage subduction history under north america inferred from multiple-frequency tomography. *Nature Geoscience*, *1*(7), 458–462.

Sigloch, K., & Mihalynuk, M. G. (2013). Intra-oceanic subduction shaped the assembly of cordilleran north america. *Nature*, *496*(7443), 50–56. Retrieved from https://doi.org/10.1038/nature12019 doi: 10.1038/nature12019

Stegman, D., Farrington, R., Capitanio, F. A., & Schellart, W. P. (2010). A regime diagram for subduction styles from 3-d numerical models of free subduction. *Tectonophysics*, *483*(1), 29–45. Retrieved from https://doi.org/10.1016/j.tecto.2009.08.041 doi: 10.1016/j.tecto.2009.08.041

Stern, T., Henrys, S. A., Okaya, D., Louie, J. N., Savage, M. K., Lamb, S., ... Iwasaki, T. (2015). A seismic reflection image for the base of a tectonic plate. *Nature*, *518*(7537), 85–88. Retrieved from https://doi.org/10.1038/nature14146 doi: 10.1038/nature14146

Strak, V., & Schellart, W. (2021). Thermo-mechanical numerical modeling of the south american subduction zone: A multi-parametric investigation. *Journal of Geophysical Research: Solid Earth*, *126*(4), e2020JB021527. Retrieved from https://doi.org/10.1029/2020JB021527 doi: 10.1029/2020JB021527

Suchoy, L., Goes, S., Maunder, B., Garel, F., & Davies, D. R. (2021). Effects of basal drag on subduction dynamics from 2d numerical models. *Solid Earth*, *12*(1), 79–93. Retrieved from https://doi.org/10.5194/se-12-79-2021 doi: 10.5194/se-12-79-2021

Torii, Y., & Yoshioka, S. (2007). Physical conditions producing slab stagnation: Constraints of the clapeyron slope, mantle viscosity, trench retreat, and dip angles. *Tectonophysics*, *445*(3), 200–209. Retrieved from https://doi.org/10.1016/j.tecto.2007.08.003 doi: 10.1016/j.tecto.2007.08.003

Tovish, A., Schubert, G., & Luyendyk, B. P. (1978). Mantle flow pressure and the angle of subduction: Non-newtonian corner flows. *Journal of Geophysical Research: Solid Earth (1978–2012)*, *83*(B12), 5892–5898.

Turcotte, D. L., & Schubert, G. (2002). *Geodynamics.* Cambridge Univ. Press, New York.

Uyeda, S., & Kanamori, H. (1979). Back-arc opening and the mode of subduction. *Journal of Geophysical Research: Solid Earth (1978–2012)*, *84*(B3), 1049–1061. Retrieved from https://doi.org/10.1029/JB084iB03p01049 doi: 10.1029/JB084iB03p01049

Van Der Meer, D. G., Spakman, W., Van Hinsbergen, D. J., Amaru, M. L., & Torsvik, T. H. (2010). Towards absolute plate motions constrained by lower-mantle slab remnants. *Nature Geoscience*, *3*(1), 36–40. Retrieved from https://doi.org/10.1038/ngeo708 doi: 10.1038/ngeo708

Van der Meer, D. G., Van Hinsbergen, D. J., & Spakman, W. (2018). Atlas of the underworld: Slab remnants in the mantle, their sinking history, and a new outlook on lower mantle viscosity. *Tectonophysics*, *723*, 309–448. Retrieved from https://doi.org/10.1016/j.tecto.2017.10.004 doi: 10.1016/j.tecto.2017.10.004

Van der Voo, R., Spakman, W., & Bijwaard, H. (1999). Tethyan subducted slabs under india. *Earth and Planetary Science Letters*, *171*(1), 7–20. Retrieved from https://doi.org/10.1016/S0012-821X(99)00131-4 doi: 10.1016/S0012-821X(99)00131-4

van Hunen, J., Huang, J., & Zhong, S. (2003). The effect of shearing on the onset and vigor of small-scale convection in a newtonian rheology. *Geophysical research letters*, *30*(19).

Wang, S., Yu, H., Zhang, Q., & Zhao, Y. (2018). Absolute plate motions relative to deep mantle plumes. *Earth and Planetary Science Letters*, *490*, 88–99. Retrieved from https://doi.org/10.1016/j.epsl.2018.03.021 doi: 10.1016/j.epsl.2018.03.021

Wu, J., Suppe, J., Lu, R., & Kanda, R. (2016). Philippine sea and east asian plate tectonics since 52 ma constrained by new subducted slab reconstruction methods. *Journal of Geophysical Research: Solid Earth*, *121*(6), 4670–4741. Retrieved from https://doi.org/10.1002/2016JB012923 doi: 10.1002/2016JB012923

Yang, T., Moresi, L., Zhao, D., Sandiford, D., & Whittaker, J. (2018). Cenozoic lithospheric deformation in northeast asia and the rapidly-aging pacific plate. *Earth and Planetary Science Letters*, *492*, 1–11. Retrieved from https://doi.org/10.1016/j.epsl.2018.03.057 doi: 10.1016/j.epsl.2018.03.057

Yang, Y., Forsyth, D. W., & Weeraratne, D. S. (2007). Seismic attenuation near the east pacific rise and the origin of the low-velocity zone. *Earth and Planetary Science Letters*, *258*(1-2), 260–268. Retrieved from https://doi.org/10.1016/j.epsl.2007.03.040 doi: 10.1016/j.epsl.2007.03.040

Zhang, H., Wang, F., Myhill, R., & Guo, H. (2019). Slab morphology and deformation beneath izu-bonin. *Nature communications*, *10*(1), 1–8. Retrieved from https://doi.org/10.1038/s41467-019-09279-7 doi: 10.1038/s41467-019-09279-7

Zindler, A., & Hart, S. (1986). Chemical geodynamics. *Annual review of earth and planetary sciences*, *14*(1), 493–571. Retrieved from https://doi.org/10.1146/annurev.ea.14.050186.002425 doi: 10.1146/annurev.ea.14.050186.002425